



**HAL**  
open science

## Mechanical feedback defines organizing centers to drive digit emergence

Carolina Parada, Samhita Banavar, Parisa Khalilian, Stephane Rigaud, Arthur Michaut, Yucen Liu, Dennis Manjaly Joshy, Otger Campàs, Jerome Gros

### ► To cite this version:

Carolina Parada, Samhita Banavar, Parisa Khalilian, Stephane Rigaud, Arthur Michaut, et al.. Mechanical feedback defines organizing centers to drive digit emergence. *Developmental Cell*, 2022, 57 (7), pp.854-866.e6. 10.1016/j.devcel.2022.03.004 . pasteur-03699969

**HAL Id: pasteur-03699969**

**<https://pasteur.hal.science/pasteur-03699969>**

Submitted on 22 Jul 2024

**HAL** is a multi-disciplinary open access archive for the deposit and dissemination of scientific research documents, whether they are published or not. The documents may come from teaching and research institutions in France or abroad, or from public or private research centers.

L'archive ouverte pluridisciplinaire **HAL**, est destinée au dépôt et à la diffusion de documents scientifiques de niveau recherche, publiés ou non, émanant des établissements d'enseignement et de recherche français ou étrangers, des laboratoires publics ou privés.



Distributed under a Creative Commons Attribution - NonCommercial 4.0 International License

## Mechanical feedback defines organizing centers to drive digit emergence

Carolina Parada<sup>1,2</sup>, Samhita P. Banavar<sup>3†</sup>, Parisa Khalilian<sup>1,2</sup>, Stephane Rigaud<sup>4</sup>, Arthur Michaut<sup>1,2</sup>, Yucen Liu<sup>5</sup>, Dennis Manjaly Joshy<sup>5</sup>, Otger Campàs<sup>5,6,7\*</sup> & Jerome Gros<sup>1,2,8\*</sup>

<sup>1</sup> Department of Developmental and Stem Cell Biology, Institut Pasteur, 75724 Paris, Cedex 15, France

<sup>2</sup> CNRS UMR3738, 25 rue du Dr Roux, 75015 Paris, France

<sup>3</sup> Department of Physics, University of California, Santa Barbara, CA 93106-5070, USA

<sup>4</sup> Image Analysis Hub, C2RT, Institut Pasteur, 75724 Paris, Cedex 15, France

<sup>5</sup> Department of Mechanical Engineering, University of California, Santa Barbara, CA 93106-5070, USA

<sup>6</sup> Department of Molecular, Cell and Developmental Biology, University of California, Santa Barbara, CA, USA

<sup>7</sup> Cluster of Excellence Physics of Life, TU Dresden, 01062 Dresden, Germany

<sup>8</sup> Lead contact

† Current address: Bioengineering department, Stanford University, CA, USA

\* Correspondence: [otger.campas@tu-dresden.de](mailto:otger.campas@tu-dresden.de); [jgros@pasteur.fr](mailto:jgros@pasteur.fr)

## Summary

5 During embryonic development, digits gradually emerge in a periodic pattern. While genetic  
evidence indicates that digit formation results from a self-organizing process, the underlying  
mechanisms are still unclear. Here, we find that convergent-extension tissue flows driven by  
active stresses underlie digit formation. These active stresses simultaneously shape cartilage  
condensations and lead to the emergence of a compressive stress region that promotes high  
10 Activin/p-SMAD/SOX9 expression, thereby defining digit organizing centers via a  
mechanical feedback. In *Wnt5a* mutants, such mechanical feedback is disrupted due to loss of  
active stresses, organizing centers do not emerge and digit formation is precluded. Thus, digit  
emergence does not result solely from molecular interactions, as previously thought, but  
requires a mechanical feedback that ensures continuous coupling between phalanx  
specification and elongation. Our work, which links mechanical and molecular signals,  
15 provides a mechanistic context for the emergence of organizing centers that may underlie  
various developmental processes.

**Keywords:** limb development, digit, phalanx-forming region/digit crescent, tissue  
mechanics, mechanobiology, mechanical feedback, chondrogenesis, organizing centers, self-  
20 organization

## Introduction

The distal-most skeletal segment of the tetrapod limb, the autopod, is composed of the carpal, metacarpal and phalangeal bones, corresponding respectively to the wrist, palm and digits of the human hand. At embryonic stage (E) 11.5 in mouse embryos, the autopod contains an iterative set of stripes expressing *Sox9* (*Sox9*<sup>+</sup>), a transcription factor necessary for cartilage condensation (Akiyama et al., 2002; Boehm et al., 2011; Montero et al., 2017). These *Sox9*<sup>+</sup> primordia prefigure the formation of the metacarpal/metatarsal bones and following phalanges (reviewed by (Montero and Hurlé, 2007)), which first appear at E12.5 (Huang et al., 2016; Witte et al., 2010).

Two mechanisms have been proposed to explain the periodic expression of *Sox9*. The first mechanism involves organizing centers, named Phalanx Forming Region or Digit Crescent (PFR/DC), located at the tip of the developing digits. These crescent-shaped organizing centers have been proposed to lead the formation of the digit ray by inducing the recruitment of distal *Sox9*-negative (*Sox9*<sup>-</sup>) mesenchymal progenitors into more proximal *Sox9*<sup>+</sup> chondrocytes (Hiscock et al., 2017; Merino et al., 1999; Montero et al., 2008). This process has been suggested to be controlled via the activation of the p-SMAD-mediated Activin/TGF- $\beta$  pathway, upstream of BMP signaling. In chick, beads soaked in Activin induce the expression of *Bmpr1b*, which is normally enriched at the PFR/DC, enabling BMP signals from the interdigital mesenchyme to promote ectopic phalanx chondrogenesis (Merino et al., 1999; Montero et al., 2008; Suzuki et al., 2008). Consistently, in mouse, mutations in *Bmpr1b* lead to digit shortening (brachydactyly) (Baur et al., 2000; Yi et al., 2000).

The second mechanism is based on the long-standing hypothesis (Newman and Frisch, 1979) that the periodic array of *Sox9*<sup>+</sup> stripes results from a self-organizing Turing-like mechanism (Turing Alan Mathison, 1952). This hypothesis has recently gained experimental support from the observation that *Hoxd11-d13;Gli3* mouse mutants exhibit polydactyly phenotypes that can be recapitulated by a Turing-type process (Sheth et al., 2012), with the associated molecular players proposed to be BMP, WNT and SOX9 (Raspopovic et al., 2014). In this model, *Sox9* expression self-organizes directly as stripes without the involvement of digit-organizing centers. A recent re-evaluation of published data attempted to reconcile these two views and proposed that digits initiate as spots (presumably via a Turing-like mechanism) that subsequently elongate into stripes, under the combined action of digit organizing centers and growth of the hand plate (Hiscock et al., 2017). However, none of these models accounts for the cellular dynamics and tissue mechanics of limb chondrogenesis, which remain unknown. Indeed, work performed on chicken and mouse limb cell cultures has suggested that in addition to signaling molecules, mechanical forces can also influence *Sox9* expression and chondrocyte differentiation (Juhász et al., 2014; Takahashi et al., 1998). However, whether mechanical forces play a similar role *in vivo* remains unknown, mostly because of the technical challenges associated with probing and manipulating the mechanical state of live embryos, especially in mouse, which develops *in utero*.

Here, using live imaging, *in situ* mechanical stress measurements, functional perturbations and computer simulations, we reveal that the endogenous mechanics of the tissue plays a fundamental role in both the control of morphogenetic flows driving digit formation and in the establishment of digit-organizing centers.

## Results

### Convergent-extension tissue flows underlie digit formation

To reveal the dynamics of digit formation, we established live-imaging conditions of the murine digit tip *ex vivo*. E11.5 limb explants expressing membrane tdTomato and/or *Sox9* reporter transgenes (*Rosa-mTmG* and *Sox9-Ires-GFP*, respectively) were cultured for 20h. From these cultured limbs (equivalent to stage E12-12.5), digit III was then imaged on a 2-photon microscope (Figure 1A-C, see also STAR METHODS and Figure S1A). The tissue flows and underlying cellular behaviors driving digit formation were analyzed using Particle Image Velocimetry (PIV) and individual cell tracking (Figure 1D-N). The measured tissue flows and cell dynamics are in agreement with static lineage studies, which previously proposed that (i) undifferentiated mesenchymal progenitors underlying the Apical Ectodermal Ridge (AER) differentiate through proximal displacement and concomitant activation of *Sox9* expression (Suzuki et al., 2008) (Figure 1E, J, M, and Videos S1-2); (ii) differentiated chondrocytes display oriented division and intercalation (Li and Dudley, 2009) (Video S3). These observations validate our *ex vivo* culture and live imaging approach.

Beyond these behaviors, our analysis reveals that mesenchymal progenitor cells under the AER move distally with rapid disorganized motion, exchanging neighbors and often moving out of the imaging focal plane, as manifested by short cell tracks and high diffusion coefficient (Figure 1E-F and J-N, Videos S1 and S4). More proximally, cells converge toward the midline of the forming phalanx where they intercalate, generating typical CE movements with characteristic hyperbolic tissue flow (and stagnation point), and two more proximolateral source-type flows (Figure 1E, G, J-N and Videos S1 and S4). The convergence site coincides with the location of digit-organizing centers (PFR/DC), where chondrogenic progenitors become specified through the activation of Activin/p-SMAD/SOX9 expression, as explained above (Figure 1I-J, L-M). SOX9<sup>+</sup> cells then move proximally in a very coherent manner, rarely exchanging neighbors, as manifested by longer cell tracks and lower diffusion coefficient (Figure 1E, H and J-N and Videos S1 and S4). Similar cell dynamics and tissue flows were observed in E12.5 + 20h limb explants (Video S5), suggesting that these behaviors are maintained throughout digit formation.

30

### WNT5A controls tissue flows, digit-organizing center emergence and subsequent phalanx formation

To evaluate the role of these newly identified CE tissue flows on digit formation, we analyzed limbs of *Wnt5a*-null mice (Yamaguchi et al., 1999), in which planar cell polarity and CE movements have been reported to be defective in numerous embryonic structures, including early limb buds (Gao et al., 2018, 2011; Gros et al., 2010; Wyngaarden et al., 2010; Yamaguchi et al., 1999). Unlike E12.5 WT embryos, whose limbs exhibit rod-shaped metacarpal cartilages and a growing first phalanx, *Wnt5a*<sup>-/-</sup> embryos display roundish metacarpals but no visible phalanx primordia (Figure 2A-B). A concomitant enlargement of the distal SOX9<sup>-</sup> population in the mutants compared to control digits (Figure 2B, E) reflects a defective chondrocyte commitment, as previously reported (Gao et al., 2011; Wang et al., 2011). By E13.5, *Wnt5a*<sup>-/-</sup> limb development is arrested at an abnormal metacarpal stage, without any digits (Yamaguchi et al., 1999) (Figure S1B-G). Live imaging of *Wnt5a*<sup>-/-</sup> limbs proved difficult because of their overall roundish shape, opacity, and increased thickness. As a result, only short time-lapse movies could be reliably analyzed. Nonetheless, PIV analysis and manual cell tracking showed that cells move in a disorganized manner and do not undergo CE movements, leading to perturbed, slow, and unsteady tissue flows with no clear

45

hyperbolic pattern, compared to control embryos (Figure 2C-C'', Video S6 and Figure S1H-I). These live observations were corroborated by segmentation-free analysis of cell anisotropy (Durande et al., 2019) performed on fixed sagittal sections of E12.5 WT and mutant limbs. In control limbs, cell anisotropy shows a gradual shift from a PD orientation in the progenitor region to an anterior-posterior (AP) orientation in the chondrocyte population (Figure 2D-D'), that aligns well with the tissue flows captured by live imaging (Figure 1L, M). In *Wnt5a*-mutant limbs, cell anisotropy is greatly reduced, with cells weakly aligned along the PD axis (Figure 2E-E'). Thus, CE movements, cellular organization and global tissue flows are defective in *Wnt5a*-mutant limbs.

We next sought to characterize the PFR/DC in *Wnt5a* mutants. For this purpose, we analyzed molecular markers that have been previously reported in both chick and mouse embryos (Huang et al., 2016; Montero et al., 2008; Suzuki et al., 2008; Witte et al., 2010). We found that in WT E12.5 limbs, *Activin*, its downstream effector phosphorylated SMAD3 (p-SMAD3), and its reported indirect target p-SMAD1/5 are highly enriched at the PFR/DC, where *Sox9* expression is activated (Figure 2F, H, J). However, in *Wnt5a*-mutant limbs, *Activin* was dramatically downregulated, with a very faint signal corresponding to metacarpal primordia (Figure 2G). Similarly, p-SMAD3 and p-SMAD1/5 showed no specific distal enrichment (Figure 2I, K). Thus, the PFR/DC is absent in *Wnt5a*-null limbs.

Previous studies in chick have revealed a central role for Activin/TGF- $\beta$  signaling in promoting phalanx formation (Merino et al., 1999; Montero et al., 2008). To confirm this role of Activin in context of the mouse digit, we treated E11.5 WT limbs for 20 h with two different pharmacological inhibitors: SB 431542, a selective inhibitor of the TGF $\beta$  type I receptors ALK5/4/7, and Sis3, a SMAD3 inhibitor. In both cases, inhibitor treatment effectively decreased p-SMAD3 activation, and lead to a strong decrease in SOX9 expression distally compared to untreated controls (Figure S2). These results confirm the critical role of Activin from the PFR/DC on the regulation of *Sox9* expression and the progression of phalanx chondrogenesis in mouse.

Previous works have proposed that the defects in chondrocyte specification in absence of *Wnt5a* or its receptor *Ror2* might be caused by an upregulation of  $\beta$ -catenin in the distal region of the digits (Gao et al., 2018; Topol et al., 2003; Witte et al., 2010; Zhu et al., 2012). Careful evaluation of  $\beta$ -catenin expression in *Wnt5a* mutants at E12.5 shows that only its membrane-associated form is increased in the distal SOX9<sup>-</sup> population, with minimal nuclear association (Figure S3A-L). N-cadherin, which binds to  $\beta$ -catenin, is also upregulated in the SOX9<sup>-</sup> distal population (Figure S3M-P), suggesting that the loss of *Wnt5a* might affect the adhesion-related function of beta-catenin rather than its transcriptional role. Furthermore, when IWP2 (a pan Wnt inhibitor) was added to WT E12.5 cultured limbs, it did not affect the pattern of *Sox9* and *Activin*, nor did it rescue their expression in *Wnt5a*<sup>-/-</sup> limbs (Figure S4C-J). However, when applied at E11.5 (prior to PFR/DC formation), IWP2 severely affected the periodic digit pattern of WT limbs (Figure S4A-B), as previously reported (Raspopovic et al., 2014), demonstrating that the treatment is effective. Altogether, these results show that the failure of chondrogenic progenitor to turn on *Sox9* expression in *Wnt5a*<sup>-/-</sup> embryos is due to the absence of digit organizing centers (PFR/DC) that cannot be attributed to an upregulation of WNT/ $\beta$ -catenin signaling.

## Mechanics of digit formation

While externally applied mechanical forces have been shown to influence *Sox9* expression and chondrocyte differentiation in cell culture (Takahashi et al., 1998), it remains

unclear whether endogenous tissue mechanics plays an important role in vivo. Since spatial variations in active force generation, tissue material properties and tissue growth can all affect tissue flows, stresses and shape (Stooke-Vaughan and Campàs, 2018), we first estimated their spatial distributions. In WT digits, Phosphorylated Myosin II (p-MyoII), a good indicator of active forces, shows no specific accumulation in distal SOX9<sup>+</sup> progenitors but is observed at the cortex of anisotropically shaped cells encompassing the PFR/DC, and also more proximally as cells maintain *Sox9* expression. Notably, p-MyoII accumulates as supracellular cables perpendicular to the PD axis of the digit, indicating that active stresses are oriented along this direction as cells initiate and maintain *Sox9* expression (Figure 3A, A' and Figure S5A for quantification).

To estimate tissue material properties, we characterized the expression of extracellular matrix (ECM) components (Hyaluronic acid (HA) and collagen 2a1 (COL2A1)) and quantified cell density, as both have been shown to influence tissue material properties (Barriga et al., 2018; Chaudhuri et al., 2020). HA, which facilitates cell movements via tissue hydration and lubrication of cell-cell and cell-matrix contacts (Solis et al., 2012), is expressed in distal progenitors and newly committed cells. In contrast, collagen, which enhances adhesion and whose expression, organization and level of mineralization is linked to increased tissue stiffness (Chaudhuri et al., 2020; Tanck et al., 2004), displays a complementary pattern in the *Sox9*<sup>+</sup> chondrocytes in WT digits (Pryce et al., 2009) (Figure 3B). These observations, together with the reported sharp decrease in cell velocity, diffusion coefficient and cell neighbor exchanges along the PD axis (Figure 1K), simultaneously indicate the existence of a distal fluid-like (low viscosity) region of progenitors/newly committed cells and a proximal solid-like (or high-viscosity) region of differentiated chondrocytes. Furthermore, we find that as cells express SOX9 and COL2A1, their proliferation decreases (Figure 3C) and their density concomitantly increases (Figure 3D, E), creating a growth (proliferation) distribution in the tissue inverse from that of tissue viscosity, with a growing fluid-like distal region and a non-growing solid-like region located more proximally (summarized in Figure 3J).

Similar analyses performed in *Wnt5a* mutant limbs reveal a high cortical accumulation of p-MyoII distally but without any sign of anisotropy nor alignment of supracellular cables, in contrast to WT digits (Figure 3F, F' and Figure S5A). Similarly, RhoA-GTP, the active form of RhoA, which is upstream of Rock/p-MyoII showed increased but disorganized signal at the cell membranes of the distal region of *Wnt5a*<sup>-/-</sup> limbs, compared to controls (Figure S5B-E). These results, which are consistent with the role of WNT5A in cell polarity acquisition (Gao et al., 2011), indicate an absence of anisotropic active stresses in *Wnt5a*-mutant limbs. Furthermore, in this distal population, which faintly expresses SOX9 (Figure 3I), proliferation and HA expression are extended proximally with complementary reduction in COL2A1 expression and a failure for cells to condense compared to WT (i.e. reduced cell density) (Figure 3E, G-I). Thus, these results suggest that in *Wnt5a* mutants, the fluid-like growing progenitor region (SOX9<sup>+</sup>; EdU<sup>+</sup>; HA<sup>+</sup>; COL2A1<sup>-</sup>) is expanded, with a shallower and smoother transition to the solid-like differentiated chondrocyte region compared to WT (summarized in Figure 3J).

### **A mechanical-feedback model for digit formation**

To explore how the emergent stresses and tissue flows could pattern the PFR/DC, we performed finite element simulations of digit formation using the obtained distributions for tissue growth, active stress, and material properties, as explained above (see also STAR METHODS and Figure S7). Simulations of WT digit formation with these input fields

(Figure 4A) not only reproduced the observed morphogenetic flows (Figure 4C) but predicted a localized region of high compressive stress (AP axial stress; Figure 4C) as the tissue transitions from a fluid to a solid state. This AP stress, localized at the tip of the developing phalanx, is reminiscent of the crescent shaped PFR/DC and congruent with high *Activin* expression (Figure 2F). These results suggested that the crescent-shaped stress localization could define the PFR/DC and drive *Sox9* expression which, in turn, would induce mesenchymal condensation and the rigidification of the tissue. We therefore implemented this mechanical feedback in the simulations, namely tissue under high compressive AP stress “solidifies” into cartilage in the next simulation iteration (see STAR METHODS). The presence of the feedback led to a nearly steady growth, with the crescent-shaped region of compressive (AP) stress resembling the PFR/DC evolving with tissue flows as observed experimentally (Figure 4C).

We next performed simulations for *Wnt5a* mutant limbs. As mentioned above, *Wnt5a* mutants display a loss of active stresses (Figure 3F, F’) as well as shallower gradients in HA expression (Figure 3G), cell proliferation (Figure 3H) and in SOX9 expression (Figure 3I) suggesting a shallower transition between fluid-like and solid-like tissue states. Simulating these conditions (Figure 4B) generates tissue flows and shape resembling those observed in *Wnt5a*<sup>-/-</sup> limbs (compare Figure 4D and 2C). Moreover, the localized region of compressive (AP) stress predicted for WT largely disappears in the absence of active stresses (Figure 4D). Indeed, simulations predict only a very weak compressive stress accumulation just distal to the solid-like region in the absence of active stresses, which is due to tissue growth as the tissue transitions from a fluid to a solid state. Implementation of the mechanical feedback leads to an isotropic expansion of the fluid-like region at the expense of the solid-like region, which evolves into a roundish shape, very much as observed experimentally in *Wnt5a*-mutant limbs.

Taken together, comparison between simulations and experimental data of WT and mutant limbs suggests that a mechanical feedback underlies digit formation. This “mechanical feedback model” makes three strong predictions: i) a localized high tissue stress emerges at the fluid-to-solid transition to define the PFR; ii) *Activin* expression, mediating the activity of the PFR/DC, should be congruent with the magnitude and localization of the emergent tissue stress to promote differentiation/solidification into cartilage; and iii) the emergence of tissue stress localization and therefore of the digit-organizing centers requires Myosin-driven anisotropic active stresses. In the following experiments, we test each of these predictions.

### **WNT5A enables emergent tissue stress at the PFR/DC**

To measure tissue stress in developing digits and test whether organizing centers are characterized by a specific stress pattern, we injected oil microdroplets (Campàs et al., 2014) with controlled bulk fluorescence and interfacial tension (i.e., calibrated droplets; see STAR METHODS and Figure S5F) at various levels along the PD axis: a distal region R1 encompassing naïve SOX9<sup>-</sup>;EdU<sup>+</sup>; an intermediate region R2 comprising SOX9<sup>+</sup>;EdU<sup>+</sup> cells and a proximal region R3 composed of SOX9<sup>+</sup>;EdU<sup>-</sup> cells (Figure 5A, G and Figure S5G). The magnitude and anisotropy of local tissue-scale stress could be deduced from droplet deformations (Mongera et al., 2018), which we acquired using 2-photon microscopy in live tissue. Analysis of tissue stress anisotropy revealed compressive stresses along the PD axis in the distal-most region (R1) of WT digits. As cells transit through the PFR/DC and turn on *Sox9* (R2), stress anisotropy changes proximally and the dominant stresses become perpendicular to the PD axis (R3; Figure 5B-E). In contrast, in the distal mesenchyme of *Wnt5a*-mutant limbs, the dominant stresses are along the PD axis in both regions R1 and R2, with the dominant stresses becoming perpendicular to the PD axis only in region R3 as cells differentiate (R3, Figure 5H-K). The difference between AP- and PD-oriented stress

magnitudes shows that AP-oriented stresses become dominant in R2 for WT, but not in *Wnt5a*-mutant limbs. Overall, our measurements reveal that compressive AP stress increases at the transition region between fluid-like/progenitor to solid-like/cartilage transition region in WT, corresponding to the PFR/DC location, whereas such stress increase is largely absent in *Wnt5a* mutants, in agreement with our model predictions.

We then checked whether *Activin* expression correlates with the localization and magnitude of the emergent stresses in WT and *Wnt5a*-mutant limbs. Sagittal sections confirmed that *Activin* is expressed at the distal end of the SOX9<sup>+</sup> condensate in WT samples, where stress accumulates (Figure 5F). In absence of *Wnt5a*, *Activin* expression relocates proximally, at the progenitor/cartilage transition region, where the emergent stress is predicted and measured to increase, although with a much lower intensity compared to WT (Figure 5L, compare with Figure 4D). Altogether, these results show that WNT5A controls the emergence of a compressive AP stress at the PFR/DC that coincides with the localization and level of *Activin* expression.

### **Actomyosin contractility is critical for the emergence of digit-organizing centers**

Finally, to directly and functionally test whether active stresses are essential to induce *Activin* expression, pattern digit-organizing centers and account for the chondrogenic defects in *Wnt5a* mutants, we inhibited Myosin II function. This was achieved by treating WT limbs with H1152, a potent inhibitor of Rock, acting downstream of RhoA to promote Myosin II phosphorylation. H1152 treatment, which leads to loss of p-MyoII without inducing toxicity (Figure S6), disrupts the CE tissue flows, with cells failing to intercalate at the PFR/DC (Figure 6A, A', Video S7). While the tissue still flows, its expansion is isotropic rather than predominantly distal, in striking resemblance with the simulated flows of *Wnt5a*<sup>-/-</sup> digits (Figure 4D). Cells fail to condense, they do not maintain *Activin* nor they induce SOX9 expression distally and do not sustain COL2A1 expression, but instead exhibit an increase in HA expression (Figure 6B-H). Therefore, disruption of active stresses using H1152, recapitulates the defects in tissue flows, cell compaction, *Activin* expression and chondrocyte specification observed in *Wnt5a* mutants.

Taken together, our results show that WNT5A controls active stresses in the tissue, which are essential to establish a crescent-shaped region of high compressive stresses in developing digits. This localized compressive stress promotes the localized and high *Activin* expression that defines digit-organizing centers, which in turn induces *Sox9* expression and sustains digit formation (Figure 7).

## **Discussion**

Mechanical forces have been shown to modulate gene expression and influence cell fate *in vitro* (Engler et al., 2006). Yet, understanding how molecular and mechanical cues interplay *in vivo* to enable organ self-organization has remained a considerable challenge (see (Hannezo and Heisenberg, 2019) for a recent review). Here, we reveal that digit formation relies on a mechanical feedback mechanism that establishes digit-organizing centers and enables the sustained elongation of digits. Our results show that the action of active stresses in the presence of a fluid-to-solid tissue transition creates a crescent-shaped region of high compressive stress at the distal fluid-to-solid boundary (Figure 7A). These localized compressive stresses induce *Activin*/p-SMAD/SOX9 expression, defining digit organizing centers and promoting phalanx cartilage differentiation, which leads to the rigidification of the tissue in this region. The local rigidification of the tissue then causes the region of high compressive stresses to progressively move distally, elongating the digit. This mechanical

feedback, which involves both active stresses and the spatial distribution of material properties in the tissue (fluid/solid transition), is molecularly relayed by Activin/p-SMAD/SOX9 (Figure 7B).

5 Our data indicates that WNT5A generates the tissue scale, anisotropic, active stresses  
necessary to create a crescent-shaped compressive stress region that modulates gene  
expression (Activin/p-SMAD/SOX9) and defines digit organizing centers, thereby enabling  
phalanx formation. Previous *in vitro* studies had shown that compressive stresses can induce  
*Sox9* in primary cell culture (Takahashi et al., 1998). Our work, which maps endogenous  
10 stresses and identifies their role in chondrocyte commitment, is consistent with these  
findings. While we do not directly address the mechanotransductive pathway linking  
endogenous stresses to *Sox9* expression activation, our results imply that modulation of the  
Activin/p-SMAD pathway mediates this effect, as *Activin*, p-SMAD, and SOX9 are  
downregulated in *Wnt5a* mutant and in H1152-treated limbs. Consistently, pharmacological  
15 inhibition of Activin signaling confirms its role in murine phalanx formation, as previously  
suggested in chick (Merino et al., 1999). In this context, BMPRI1B pathway, downstream of  
Activin is at the intersection between the activities of digit (PFR/DC) and interdigital  
signaling centers (Huang et al., 2016; Merino et al., 1999; Suzuki et al., 2008), in which  
*5'Hoxd-Gli3* dosage sets up net BMP signaling levels, to promote phalanx-interzone  
formation and hence phalanx periodicity (Huang et al., 2016).

20 In addition, we find that as metacarpals condensations are being established, the  
WNT5A-controlled anisotropic active stresses power the concomitant CE tissue flows,  
driving digit elongation and morphogenesis. In absence of *Wnt5a*, the metacarpal cartilage  
condensations bear a roundish morphology. This finding is in support of the proposition that  
the most distal elements of the autopod initiate as spots and elongate into stripes (Hiscock et  
25 al., 2017). However, our results show that digit elongation is not driven solely by growth, as  
previously thought (Hiscock et al., 2017; Marcon et al., 2011; Raspopovic et al., 2014), but  
rather by active and oriented stresses/cell behaviors.

Our results also uncover several sequential mechanisms underlying digit formation.  
Consistent with the proposition that metacarpal and phalanges are controlled by distinct  
30 developmental modules (Kavanagh et al., 2013), we found that metacarpal and phalanx  
formation involve distinct mechanisms and can be decoupled, as observed in *Wnt5a* mutants.  
Our data argue that while a Turing-like mechanism may be responsible for the periodic  
pattern of metacarpals (which compose the palm/paw), it is the emergence of organizing  
centers via a mechanical feedback that actually triggers the ensuing digit formation  
35 (phalanges), as recently speculated (Hiscock et al., 2017). Further support on this conclusion  
is the inhibition of the WNT/ $\beta$ -catenin pathway, which alters the digit periodic pattern only  
before the emergence of the PFR/DC at E11.5 (Raspopovic et al., 2014) but not at E12.5,  
although phalanges are forming. Thus, whereas digit formation builds on the metacarpal  
periodic pattern, the formation of phalanges themselves is independent of a Turing-type  
40 mechanism. It is worth mentioning that the PFR/DC is not only essential for the transition  
from metacarpal cartilage to first phalanx but also for the addition of new segments to the  
digit. Consistently, Witte et al. (2010) showed that alterations in the PFR/DC  
in *Ror2*<sup>W749X/W749X</sup> mutants lead to disruption in the development of phalanges 2 and 3,  
although phalanx 1 is normal. In light of our findings, it is possible that the mechanical  
45 feedback described herein is present, but weaken, in *Ror2* mutants, leading to a milder  
phenotype than in *Wnt5a*-mutant mice.

In sum, our work clarifies the cellular, molecular, and mechanical processes  
underlying digit emergence, placing mechanical forces as a critical signal coordinating

phalanx specification and elongation. Our results indicate that digit organizing centers arise as an emergent property of the tissue, through a mechanical feedback on the coexistent signaling pathways. Taken broadly, our data highlight the need to integrate molecular, cellular, and mechanical aspects, along with their reciprocal feedbacks, to understand how organs self-organize during development.

### *Limitations of the study*

Our analyses of tissue flows were performed in two dimensions (2D) since acquiring digits in both three dimensions (3D) and time at exploitable spatiotemporal resolutions was not possible using ‘conventional’ two-photon live microscopy. The analysis of cell polarity in transverse and sagittal section throughout this study suggests that the tissue flows we brought to light at the distal limb, as well as expression patterns are rotationally symmetrical around the digit axes. However, future experiments capturing digit formation in 3D and in time will be necessary to confirm this aspect since digits are three-dimensional structures. Similarly, we simulated a 2D section of the system because three dimensional simulations were too computationally complex. Since the physics of the problem is the same in 2D or 3D and because a single digit is approximately rotationally symmetric, we do not expect qualitative changes in the results, but 3D simulations could lead to more quantitatively accurate results. We simulated a single digit for simplicity, but it would be interesting to study the mechanical coupling between digits, as this could affect the spatiotemporal pattern of stresses for larger tissue deformations at longer timescales. Moreover, whereas digits are segmented into successive phalanges, our model of digit formation via a mechanical feedback does not take this aspect into consideration. Only addition of cartilage distally (corresponding to the induction of *Sox9* expression at organizing centers) is accounted for in our model. More work will be necessary to evaluate the role of mechanical forces in the segmentation of digits into phalanges and in the formation of synovial joints.

### **Acknowledgments**

We thank Francis Corson for critical feedback and for sharing PIV analysis tools, Sangwoo Kim (UCSB) for sharing image analysis codes, Ellen Sletten (UCLA) for sharing custom-made fluorinated dyes, and Yang Chai (USC) for providing us with the plasmids for *Sox9* and *Activin AB* probes. This work was supported by a Research Grant from HFSP (Ref. No: RGY0067/2015 to OC and JG) and by Laboratoire d'Excellence Revive (Investissement d'Avenir; ANR-10-LABX-73 to JG). OC was also partially supported by the Deutsche Forschungsgemeinschaft (DFG, German Research Foundation) under Germany's Excellence Strategy – EXC-2068 – 390729961.

### **Author contributions**

Conceptualization: CP, JG, OC

Methodology: CP, SPB, JG, OC

Formal analysis: CP, SPB, PK, SR, AM

Investigation: CP, SPB, PK

Resources: YL, DMJ

Visualization: CP, SPB, JG, OC

Funding acquisition: JG, OC

Writing – original draft: CP, JG

5 Writing – review & editing: CP, SPB, JG, OC

### **Declaration of interests**

Authors declare that they have no competing interests.

10

## **Main figure titles and legends**

### Figure 1. Dynamics of digit chondrogenesis.

(A) Scheme of the live imaging set up. See Figure S1 for more details on the method.

(B) Dorsal view of an E11.5 limb explant cultured for 20h prior to imaging (t0). Dashed box: region imaged.

5 (C) *Rosa<sup>mTmG/mTmG</sup>; Sox9<sup>IRES-GFP/IRES-GFP</sup>* digit expressing tdTomato membrane and GFP *Sox9* reporters at t0.

(D and E) Membrane reporter at t0 (D) and t16h (E) with color-coded cell tracks overlaid.

10 (F to H) Tracking of mesenchymal cells for 4 hours at different regions along the PD axis, as indicated in (D), showing disorganized and out-of-the plane movements (F-F'), oriented intercalation (G-G') and coherent movements with no local neighbor exchange (H-H'). See also Videos S1 and S4.

(I and J) GFP reporting *Sox9* expression at t0 and at t16h (J) with color-coded cell tracks overlaid. See also Video S2.

15 (K) Quantification, along the PD axis of cell velocity (red) and diffusion coefficient (blue) obtained from cell tracking data, and SOX9 expression (green). 0 corresponds to the distal-most point. Data are represented as mean  $\pm$  SEM.

(L and M) Tissue flows obtained by PIV analysis, showing streamlines and color-coded speed at t+24 (L) and velocity fields overlaid on *Sox9-ires-GFP* reporter at t16h (M). Red dots in velocity field indicate topological defects in the flow field.

20 (N) Quantification of velocity along the PD (y) axis from individual cell tracking data (red) and PIV of three different limbs (A, B, C, in blue, green, and orange), showing consistence between the two methods. Data are represented as mean  $\pm$  SEM.

Scale bars: B: 100  $\mu$ m, C-E and I-K: 50  $\mu$ m and F-H: 10  $\mu$ m. Abbreviations: A: anterior, D: dorsal, V: ventral, Di: distal, Po: posterior, Pr: proximal.

25

### Figure 2. Altered tissue flows, defective chondrogenesis, and absence of PFR/DC in *Wnt5a*<sup>-/-</sup> limbs.

30 (A and B) Whole-mount immunofluorescence against SOX9 on E12.5 control (A) and *Wnt5a*-mutant limbs (B), showing defects in phalanges formation and shape of metacarpal primordia (n=4 WT, n= 4 *Wnt5a*<sup>-/-</sup> limbs). See Figure S1B-G for other stages.

(C) E12.5 *Wnt5a*<sup>-/-</sup>; *Rosa<sup>mTmG/mTmG</sup>* cultured for 20h prior to live imaging (t0) and tissue flows obtained by PIV analysis, showing streamlines and color-coded speed at t0 (C') and t+2h (C''), showing slow and unsteady tissue motion. See also Video S6 (n=3 *Wnt5a*<sup>-/-</sup> limbs) and Figure S1H-I for a projection of individual cell tracks.

35 (D and E) Cell anisotropy analysis on sagittal sections of E12.5 control and mutant limbs. Angles are plotted in D', E' (n=10 WT, n=10 *Wnt5a*<sup>-/-</sup> limbs). Red arrowhead on D points to the proximal end of the PFR/DC (P1).

(F and G) *Activin* in situ hybridization of E12.5 control and *Wnt5a*<sup>-/-</sup> limbs, showing positive signal at the PFR/DC in control and weaker signal at the level of the MC in mutant limbs (n=5 WT, n=6 *Wnt5a*<sup>-/-</sup> limbs).

40 (H and I) P-SMAD3 color-coded immunofluorescence on sagittal sections of control (H) and *Wnt5a*<sup>-/-</sup> limbs (I) (n= 5 WT, n=5 *Wnt5a*<sup>-/-</sup> limbs).

(J and K) P-SMAD1/5 color-coded immunofluorescence on sagittal sections of control (J) and *Wnt5a*<sup>-/-</sup> limbs (K) (n= 5 WT, n=6 *Wnt5a*<sup>-/-</sup> limbs).

45 Scale bars: 500  $\mu$ m (A-B), 50  $\mu$ m (C), 100  $\mu$ m (D-E and H-K) and 200  $\mu$ m (F-G). Abbreviations: MC: metacarpal bone primordium, P1: first-phalanx primordium, PH: phalloidin.

### Figure 3. Contribution of tissue mechanics to chondrogenesis and PFR/DC emergence.

(A, A' and F, F') Phospho-Myosin II immunofluorescence of the distal tip of digit III in E12.5 control and *Wnt5a*<sup>-/-</sup> limbs; Yellow arrowhead point at distal cells with no particular p-MyoII accumulation, Arrows point to supracellular p-MyoII cables aligned along the AP axis (n=3 WT, n=3 *Wnt5a*<sup>-/-</sup> limbs). For p-MyoII quantification see Figure S5A.

5 (B and G) Hyaluronic acid and collagen 2a1 immunofluorescence of control (B) and *Wnt5a*<sup>-/-</sup> (G) limbs (n=3 WT, n=3 *Wnt5a*<sup>-/-</sup> limbs).

(C and H) EdU staining and SOX9 immunofluorescence of control (C) and *Wnt5a*<sup>-/-</sup> (H) limbs (n=3 WT, n=3 *Wnt5a*<sup>-/-</sup> limbs).

10 (D and I) Hoechst staining and SOX9 immunofluorescence of control (D) and *Wnt5a*<sup>-/-</sup> (I) (n=9 WT, n=8 *Wnt5a*<sup>-/-</sup>). Note reduced cell density in the distal region of the *Wnt5a*-mutant sample.

(E) Quantification of cell density of control and *Wnt5a*<sup>-/-</sup> limbs (n=9 WT, n=8 *Wnt5a*<sup>-/-</sup>). Data are represented as mean ± SD.

15 (J) Sketch summarizing the distribution of active forces, growth, and material properties with respect to chondrocyte differentiation in WT and *Wnt5a*<sup>-/-</sup> limbs, as estimated from immunofluorescence and quantitative live imaging analysis. All immunofluorescence images shown in this figure are sagittal sections.

Scale bars are 50 μm.

20 **Figure 4. Simulations of digit formation in the presence of mechanochemical feedback.**

(A and B) Input (initial) spatial distributions of cell proliferation (growth  $Q(\vec{x})/Q_0$ , with  $Q_0$  being the maximal cell proliferation rate), active stress ( $A(\vec{x})/\sigma_{SF}$ , with  $\sigma_{SF}$  being the shear stress scale in the fluid-like tissue region), and tissue viscosity ( $\mu(\vec{x})/\mu_F$ , with  $\mu_F$  being the viscosity scale in the fluid-like region) for WT (A) and *Wnt5a* mutants (B).

25 (C and D), Simulated time evolution of the velocity field ( $\vec{v}(\vec{x})/v_0$ , with  $v_0$  being the velocity scale; streamlines shown; magnitude, color coded), stress in the AP direction ( $\sigma_{AP}(\vec{x})/\sigma_{SF}$ ), and tissue viscosity ( $\mu(\vec{x})/\mu_F$ ) for WT (C) and *Wnt5a* mutants (D). Red dots in velocity field indicate topological defects in the flow field.

See STAR METHODS and Figure S7 for definitions of all theoretical quantities.

30 **Figure 5. WNT5A enables emergent tissue stress at the PFR/DC**

(A and G) EdU staining and SOX9 immunofluorescence on sagittal sections of control (A) and *Wnt5a*<sup>-/-</sup> samples (G), which are high magnifications of Figure 3C and H, displaying regions R1, R2, R3 used for the quantifications.

35 (B and H) Image of a single droplet injected in regions R1, R2, or R3 in control (B) and *Wnt5a*<sup>-/-</sup> limbs (H) and rosette plots of long-axis orientation for all injected droplets (n=37 droplets in WT, 22 droplets in *Wnt5a*<sup>-/-</sup>). See also Figure S5G.

(C and I) Average angle ( $\theta$  of droplet long-axis relative to PD axis in control (C) and *Wnt5a*<sup>-/-</sup> (I).

40 (D and J) Magnitude of anisotropic stress along the PD and AP axis.

(E and K) Schemes summarizing stress anisotropy, deduced from droplet deformation (pink ellipse) relative to *Sox9* expression.

(F and L) Sagittal sections of WT (F) and *Wnt5a*<sup>-/-</sup> (L) limbs showing *Activin* (red) and SOX9 (green) expression, as well as Hoechst staining (blue) (n= 3 WT, n=3 *Wnt5a*<sup>-/-</sup> limbs).

45 Scale bars are 50 μm

**Figure 6. Actomyosin contractility is critical for the emergence of digit organizing centers.**

- (A) E12.5 limbs treated with H1152 and altered tissue flows as revealed by streamlines and color-coded velocity (A') (n=3 H1152-treated limbs).
- 5 (B and C) In situ hybridization showing decreased *Activin* expression in H1152-treated limbs (C) compared to control digits (B) (n=5 control, n=5 H1152-treated limbs).
- (D and E) Immunofluorescence on transverse sections showing decrease in collagen 2a1 expression and concomitant increase in HA expression upon H1152 treatment compared to control limbs (n=5 control, n=3 H1152-treated limbs).
- 10 (F and G) Hoechst staining and SOX9 immunofluorescence on transverse sections of control (G) and H1152-treated digits (F). Note the defect in activation of SOX9 expression (brackets) upon H1152 treatment compared to control limbs (n=6 control, n=3 H1152-treated limbs).
- H, Quantification of cell density of control and H1152-treated digits (n=6 untreated control, n=3 H1152-treated limbs). Data are represented as mean  $\pm$  SD.
- 15 See also Figure S6 for the effect of H1152 on p-Myosin II and cell survival.
- Scale bars are 50  $\mu$ m.

**Figure 7. Mechanical feedback model for the emergence of digits.**

- (A) In WT, active stresses in the presence of a fluid-to-solid transition creates a crescent shaped region of high compressive stresses, which induces high *Activin* expression, defining digit organizing centers. In absence of *Wnt5a* (i.e., altered anisotropic active forces), convergent-extension tissue flows do not occur, the compressive stress region does not emerge, *Activin* is not induced at correct levels, the tissue only weakly “solidifies”/differentiates, and as a result digit never emerge.
- 20
- 25 (B) Diagram summarizing the mechanical feedback, which consists of high compressive stress (enabled by the combined action of active stresses and the spatial distribution of material properties – solid/fluid states) causing the rigidification of the tissue through the activation of *Activin/SOX9/COL2A1* expression.

## STAR METHODS

### RESOURCE AVAILABILITY

#### *Lead contact*

5

Further information and requests for resources and reagents should be directed to and will be fulfilled by the lead contact, Jerome Gros (jerome.gros@pasteur.fr).

#### *Materials availability*

10

This study did not generate new unique reagents.

#### *Data and code availability*

15

- All data reported in this paper will be shared by the lead contact upon request.
- Original code for the analysis of cell tracking was deposited at GitLab. A method paper including this code is in preparation. A link to this code is provided in the key resources table.

20

Analyses of cell shape and p-Myosin II anisotropy were performed using the segmentation-free Fourier-transform-based method proposed by Durande et al. (Durande et al., 2019), whose code can be found at GitHub. Extension to that code relevant to our analyses is available at Zenodo. Its DOI is listed in the key resources table.

25

These codes are all publicly available as of the date of publication.

30

Original codes for the PIV analyses and finite element simulations are available upon request.

- Any additional information required to reanalyze the data reported in this paper is available from the lead contact upon request.

35

### EXPERIMENTAL MODEL AND SUBJECT DETAILS

#### *Mouse husbandry and breeding*

40

B6;129S7-*Wnt5a*<sup>tm1Amc</sup>/J (RRID:MGI:4830969; Yamaguchi et al., 1999) and *Gt(ROSA)26Sor*<sup>tm4(ACTB-tdTomato,-EGFP)*Luo*</sup>/J (RRID:MGI:3716464; Muzumdar et al., 2007) strains of mice were purchased from The Jackson Laboratory. *Sox9-Ires-GFP* (B6;129S4-*Sox9*<sup>tm1.1Tlu</sup>/J) heterozygous mice initially generated in Dr. Lufkin's laboratory (RRID:IMSR\_JAX:030137; Chan et al., 2011) were transferred from Dr. Zeller's laboratory.

45

All procedures using animals were approved by the ethics committee of Pasteur Institute (CETEA, Protocol Number HA0040) and were performed according to the European Community guidelines. *Wnt5a*<sup>+/-</sup> mice were crossed with homozygous *Rosa-mTmG* mice to

generate a  $Wnt5a^{+/-};Rosa^{mTmG/mTmG}$  stock, which was then interbred to obtain pregnant females carrying  $Wnt5a^{-/-};Rosa^{mTmG/mTmG}$  mutant embryos.  $Rosa-mTmG$  embryos were obtained by crossing homozygous mice.  $Sox9-Ires-GFP$  mice were also kept as a homozygous stock and interbred to obtain homozygous embryos. E11.5, E12.5, and E13.5 embryos were used.

## METHOD DETAILS

### *Limb culture and pharmacological treatments*

$Rosa^{mTmG/mTmG}$ ,  $Sox9^{Ires-GFP/Ires-GFP}$ , or  $Wnt5a^{-/-};Rosa^{mTmG/mTmG}$  embryos were dissected from timed-pregnant mice at E11.5 or E12.5. Limbs were microdissected in pre-warmed sterile PBS and placed immediately in a pre-warmed culture medium containing DMEM:F12, 20% FCS, and 100U penicillin/ml and 0.1 mg streptomycin/ml. Limbs were then transferred to PET transparent inserts, pore size 1  $\mu$ m, for 12-well plates (Falcon Corning). Two limbs were placed in each insert with their dorsal side facing the membrane. They were then cultured in a 37C incubator under an atmosphere of 5% CO<sub>2</sub> for 20h before live imaging or for 3h to 20h for pharmacological treatments (Figure S1A). Pharmacological treatments were performed by supplementing the culture medium with IWP2 (10  $\mu$ M, Tocris, Biotechne), H1152 (2.5  $\mu$ M, Tocris-Biotechne), SB 431542 (50  $\mu$ M, Tocris-Biotechne), Sis3 (30  $\mu$ M, Tocris-Biotechne) and DMSO or water as negative control, for 20h for immunostaining or in situ hybridization experiments.

### *Live imaging and image analysis*

Cultured limbs were transferred over a LabTek 35 mm glass-bottom culture dish containing a 1 mm-thick 1% low-melting agarose layer, prepared with the above-mentioned culture medium. Briefly, the dish was incubated for an hour in the incubation chamber of a Zeiss LSM 7MP inverted 2-photon microscope at 37C, passive humidity, and 5% CO<sub>2</sub>, prior to imaging. In the case of H1152 treatments, limb explants were incubated with 2.5  $\mu$ M H1152-supplemented liquid medium for 3h before live imaging. The agarose layer used for imaging was supplemented with the same concentration of H1152. Only digit III was imaged. Typically, z-stacks were acquired every 12-30 minutes for around 5-24h, using a Plan-Apochromat 40x objective at a wavelength of 850 nm for GFP and 1100 for Tdtomato owing to a Chameleon TiSaph laser and OPO device from Coherent. In most cases, the limbs were fixed after imaging for SOX9 immunostaining.

Individual cell tracking and cell division quantifications were performed manually on registered time-lapse movies using Fiji as previously described (Gros et al., 2010; Romereim et al., 2014; Schneider et al., 2012). Regarding, cell movement quantifications, instantaneous velocities were calculated by computing the discrete time derivative of positions along individual trajectories, using a second order accurate central differences method provided by gradient function from the Python package Numpy (Harris et al., 2020). Diffusion coefficients were calculated by fitting the mean squared displacement (MSD) with a biased random walk model. The MSD was calculated using the overlapping intervals method (Dickinson and Tranquillo, 1993): we write  $\Delta r(\tau)$  the displacement between two points of the trajectory separated by a time interval  $\tau$ , then the MSD is the mean of the squared displacement over every pairs of points along the trajectory, noted  $\langle \Delta r^2(\tau) \rangle$ . Since our cells exhibit a random walk within a flow of velocity  $v_{flow}$ , the MSD follows:

$\langle \Delta r^2(\tau) \rangle = 4D\tau + v_{flow}^2\tau^2$  where  $D$  is the 2D diffusion coefficient. Then, the MSDs of all trajectories within three regions of interest were averaged together to be fitted with the biased random walk model using the Python fitting package LMFIT (Newville et al., 2016). As MSD statistic decreases as lag times  $\tau$  increases, we fitted the biased random walk model for  $\tau < 50$  min.

Particle image velocimetry (PIV) was used to evaluate the local displacement of the tissue between successive movie frames. The resulting displacement fields were used to identify velocity fields and streamlines as described in Banavar et al. (Banavar et al., 2021), and Saadaoui et al. (Saadaoui et al., 2020). A quantification of velocity was performed from the PIV data of three different imaged limbs and compared to the individual cell manual tracking to validate the PIV analysis (Figure 1).

### *Immunostaining, EdU essay, cell density analysis and cell anisotropy analysis*

For immunostaining on sections, fixed limbs were embedded in 7.5% gelatin/15% sucrose and sectioned sagittally or transversally using a Leica CM3050S cryostat. Sections were degelatinized in PBS at 37C for 30 min and blocked in PBS/0,1% Triton/10% goat serum for one hour at RT. Sections were then incubated with primary antibodies to (Pan)  $\beta$ -catenin (1/200, BD Transduction laboratories), Collagen 2a1 (1/50, Abcam), N-cadherin (1/200, Sigma-Aldrich), p-Myosin II (1 /75, Cell Signaling technology), p-SMAD1/5 (1 /50, Cell Signaling technology), p-SMAD3 (1/200, Abcam), RhoA-GTP (1:300, Neweast Biosciences) and/or SOX9 (1 :1000, EMD Millipore) overnight at 4C. Afterwards, they were washed for 1h with PBS/0,1% Triton and incubated 2h at RT with Alexa Fluor 488, 555, and/or 647 secondary antibodies (1/400, Invitrogen). After washing with PBS/0,1% Triton, sections were stained with Hoechst (1/10000, Invitrogen) and mounted in Fluoromount G (eBiosciences). P-SMAD1/5 immunostaining required methanol permabilization prior to the blocking step. p-Myosin II primary and secondary antibody incubation was performed using Can Get Signal™ immunostain enhancer solution (TOYOBO). Heat-induced epitope retrieval with citrate buffer (Sigma) was performed for Collagen 2a1 immunostaining. Alexa Fluor 647 Phalloidin (1/100, Invitrogen) was used for actin staining. Hyaluronic acid staining was performed using Hyaluronic Acid Binding Bovine Nasal Cartilage biotinylated FDS (1/200, EMD Millipore) and Alexa Fluor 647 streptavidine (1/400, Invitrogen). Images were acquired using an inverted confocal microscope (Zeiss LSM700).

For whole-mount immunostaining, fixed limbs were dehydrated in an increasing series of methanol and stored for at least three days in 100% methanol at -20C. They were rehydrated, washed overnight with PBS/0,2% Triton and blocked overnight in PBS/0,2% Triton/10% goat serum/0.5% BSA. Afterwards, limbs were incubated with primary antibody (SOX9, using the same dilution as on sections) in blocking buffer at 4C for five days and subsequently washed overnight with PBS/0,2% Triton. Incubation with the secondary antibody was carried out for three days in blocking buffer at 4C. Limbs were then washed overnight with PBS/0,2% Triton and cleared using ScaleA2 for a week. Images were acquired using a SteREO Discovery.V8 macroscope (Zeiss).

Cell proliferation was evaluated in vivo by EdU labeling (5-ethyl-2'-deoxyuridine, Invitrogen E10187). EdU was injected intraperitoneally to pregnant females at 30  $\mu$ g/g body

weight (6 mg/ml solution in 0.9% saline) two hours before sacrificing them. Embryos were dissected out and their limbs fixed and processed for gelatin sections. EdU detection was performed using the Click-iT EdU Cell Proliferation assay kit (BCK-EDU488, Sigma-Aldrich) following the instructions of the manufacturer. Cell density was determined using Hoechst staining along the PD axis on sagittal and transverse sections.

Analyses of cell anisotropy were performed using the segmentation-free Fourier-transform-based method proposed by Durande et al. (Durande et al., 2019), which computes a coarse-grained spatial analysis on a membrane signal. Phalloidin staining in E12.5 WT and *Wnt5a*<sup>-/-</sup> limbs was carried out for this purpose. The limb epithelium was not included in the analysis. The digit mesenchyme was divided into two regions of interest: SOX9<sup>-</sup> and SOX9<sup>+</sup> cells. Analyses of p-Myosin II orientation were performed using the same pipeline.

### ***In situ hybridization***

Limbs were fixed in 4% formaldehyde, dehydrated and stored in 100% methanol. They were then treated with Proteinase K (10 mg/mL) and refixed with 4% formaldehyde/0,1% glutaraldehyde. Hybridization with DIG-labeled RNA probe was performed under stringent conditions at 65°C. Washed limbs were treated with MABT/2% BBR/20% Lamb Serum and incubated overnight with AP-coupled anti-DIG antibody. Limbs were then stained with NBT/BCIP liquid substrate (Sigma). Pictures were taken using a microscope (SteREO Discovery.V8, ZEISS) with a 1X objective and a color camera (AxioCam MRc, Zeiss). DIG-labeled probes were generated from plasmids containing cDNA fragments of *Activin AB* and *Sox9* (gifts from Y. Chai, USC).

### ***Droplet injection, imaging and calibration***

Oil droplets were generated in a similar way as previously described (Mongera et al., 2018). Fluorescently labeled 3M Novec 7700 fluorocarbon oil (with a fluorinated Rhodamine dye and a fluorinated surfactant diluted in it; see below) was directly injected in E12-E12.25 WT and *Wnt5a*<sup>-/-</sup> limbs along the PD axis in digits II, III and IV, using a pressure controlled microinjector. The required droplet size (of average diameter ranging between 30-60 μm) was achieved by modulating the injection pressure and the injection pulse interval. To prevent non-specific adhesion at the droplet surface and control the interfacial tension, a fluorinated Krytox-PEG (600) surfactant (008-fluorosurfactant, RAN Biotechnologies) was diluted in the Novec 7700 oil at a 2% (w/w) concentration. In addition, in order to visualize the droplets using fluorescence microscopy, droplets were labelled using a custom-synthesized fluorinated Rhodamine dye (Sletten and Swager, 2014), which was diluted in the Novec 7700 oil at a final concentration of 25 μM. After injection, limb explants were cultured as described above (see limb culture section) for a period of six hours to allow tissue recovery before imaging. Droplets were imaged using a Zeiss LSM 7MP inverted 2-photon microscope. To establish the position of the droplets along the PD and AP axis, we defined the digit/metacarpal contours and the midline as landmarks on transmitted light images. We then measured the distance between the center of the droplet to these landmarks (Figure S5).

In order to calibrate the droplets, it is necessary to know their interfacial tension  $\gamma$ , which we measured using a pendant drop tensiometer (Theta Lite, Biolin Scientific), as previously described (Lucio et al., 2017) (Figure S5). Briefly, the interfacial tension of

fluorinated oil Novec 7700 containing 2% (w/w) Krytox-PEG(600), both in the presence and absence of 25  $\mu\text{M}$  of fluorinated Rhodamine, was measured in Milli-Q water and also in tissue culture media (RPMI supplemented with 10% Fetal Bovine Serum and 1% PenStrep). In all cases, the interfacial tension was measured to be close to 5 mN/m, indicating that the fluorinated surfactants maintain the interfacial tension constant even with strong changes in ionic strength and in the presence of other small molecules and proteins in solution, as previously shown for different oil droplets (Lucio et al., 2017). Since our experiments are in tissue culture media, we used the measured interfacial tension value of  $\gamma=5.2$  mN/m for our stress measurements (Figure S5).

### ***Stress measurements***

Stresses were obtained from droplet deformations as previously reported (Mongera et al., 2018). Briefly, to quantify tissue-scale (supracellular) stresses, we fitted an ellipse to the measured droplet shape using ImageJ. The value of anisotropic tissue stresses for the ellipsoidal droplet deformation is given by  $\sigma_T^A = 2\gamma(H_b - H_a)$ , where  $H_b$  and  $H_a$  are the mean curvatures of the droplet at the intersection of the two principal axis with the ellipsoid and  $\gamma$  is the droplet's interfacial tension. The mean curvatures  $H_b$  and  $H_a$  are given by  $H_b = b/a^2$  and  $H_a = (1/2) a + a/(2b^2)$ , with  $b$  and  $a$  being the long and short semi-axis of the fitted ellipse, respectively. To obtain the direction of droplet deformation, we measured the angle between the direction defined by the long axis of elliptical droplet deformation and the PD axis of the embryo using ImageJ.

### ***Simulations***

In order to simulate digit morphogenesis, we restrict ourselves to the growth of an emerging single prospective digit (Figure S7A, A'). At supracellular length scales and developmental time scales, tissues can be physically described as continuum materials. At these length- and time-scales, coarse-grained continuum approaches are best suited to simulate tissue morphogenesis, and several previous works have used these simulation methods in other systems (Banavar et al., 2021; Mongera et al., 2018; Tanaka, 2015; Wyczalkowski et al., 2012). Since we are interested in tissue-scale morphogenesis, we use this continuum approach and simulate the physical expansion of a 2D dorsoventral projection of the emerging mouse digit. While the dynamics of the system is governed by general conservation laws (mass and momentum conservation; see below), there are several physical fields that need to be phenomenologically determined as these are not constrained by physics and, instead, they are determined by the biological system in question (Stooke-Vaughan and Campàs, 2018). These physical fields, namely the tissue growth (cell proliferation), the active stress (actomyosin-generated supracellular stress), and the tissue material properties, are input fields in these simulations and must therefore be determined experimentally.

We estimated these input fields from the experimental data (see main text and below). The spatial distribution of tissue growth was inferred from EdU labeling (Figure 3A and Figure S7B), which indicated the existence of a proliferative region next to the ectoderm in the emerging digit, with a largely non-proliferative region defined by Sox9<sup>+</sup> cells. We defined the length scale of this proliferative region as  $\lambda$  (Figure S7B). The spatial profile of tissue material properties was deduced from differential cell behaviors (Figure 1F-H, Video S1 and Figure S7B), cell density and expression of molecular markers (e.g. Col2a1 and HA, see

Figure 3B-D), which all simultaneously indicate the existence of a fluid-like (low viscosity) progenitor region in the tissue and a solid-like (or high-viscosity) tissue region of committed chondrocytes. Since the solid-like region largely coincides with the Sox9<sup>+</sup> region, we use the same length scale  $\lambda$  to characterize the location of the fluid-to-solid transition in the tissue (Figure S7B). Finally, the spatial distribution of active stresses was deduced from p-MyoII immunofluorescence (Figure 3I), endogenous tissue stress measurements (Figure 3E-H), and cell shape anisotropy (Figure 2D, D', E, E'). The oriented, supracellular myosin cables in the Sox9<sup>+</sup> region (and their absence when myosin activity is disrupted), and the largely disordered actomyosin structures in the proliferative region of the tissue, suggest that active stresses are present in the Sox9<sup>+</sup> region only and are directed in the perpendicular direction to the PD axis (Figure S7B). Direct measurements of stresses support this assumption, and they show the appearance of large stresses in the direction perpendicular to the PD axis in the Sox9<sup>+</sup> region. Because all input fields could be characterized by a spatial distribution with one region for distances smaller than  $\lambda$  from the ectoderm of the emerging digit and a distinct region for distances larger than  $\lambda$ , and because the emerging digit has a geometry that resembles a semi-circle, we simplified the spatial structure of the input field to reflect these features (Figure S7B).

To simulate tissue morphogenesis from these input fields, we describe the tissue as a viscous fluid with inhomogenous viscosity (viscosity field as indicated above; Figure S7B), as previously done for other developmental systems (Banavar et al., 2021; Mongera et al., 2018). The dynamics of the tissue is governed by two fundamental physical laws, namely momentum conservation (which reduces here to local force balance because inertial terms are negligible for embryonic tissues) and mass balance, which read

$$\nabla \cdot (\sigma_P + \sigma_A) = 0, \quad (S1)$$

$$\nabla \cdot \mathbf{u} = \frac{Q}{\rho}, \quad (S2)$$

where  $\sigma_P$  and  $\sigma_A$  are the passive and active stress tensors, respectively,  $\mathbf{u}$  is the tissue velocity,  $\rho$  is the tissue density and  $Q$  is the cell proliferation rate. Since changes in cell density can lead to strong changes in tissue fluidity, for simplicity we only account for the effect of cell density in changes of material properties, but otherwise assume the cell density constant in the tissue. The constitutive equation, relating the passive stresses in the tissue to the strain rates (and flows), can be written as

$$\sigma_P = -p\mathbf{I} + \mu(\nabla\mathbf{u} + \nabla\mathbf{u}^T - (\nabla \cdot \mathbf{u})\mathbf{I}) \quad (S3)$$

where  $\mathbf{I}$  is the identity tensor,  $p$  the tissue pressure and  $\mu$  the tissue viscosity. In order to completely determine the problem, it is necessary to specify the boundary conditions. In these simulations, the tissue boundary is not imposed or fixed (free boundary problem), but rather the tissue shape is an outcome of the simulations. At the boundary, local normal forces must balance and velocities must be continuous, as previously done in similar free boundary problems (Banavar et al., 2021; Mongera et al., 2018). Local normal force balance (equivalent to Laplace's Law) reads

$$\Delta\sigma_{nn} = \Gamma\kappa \quad (S4)$$

where  $\Delta\sigma_{nn}$  is jump in normal stress (along the normal direction) at the tissue boundary,  $\Gamma$  is the tissue surface tension and  $\kappa$  is the curvature of the tissue surface. For simplicity, we

assume the tissue surface tension to be uniform and constant. Outside the tissue, we simulate a fluid with a viscosity negligible compared to the viscosity of the tissue to capture the presence of cell culture media (tissue viscosities are typically at least  $10^5$  times that of water, or cell culture media).

5

The input scalar fields  $Q(\vec{x})$  and  $\mu(\vec{x})$  correspond to the spatial profiles of cell proliferation and tissue viscosity, respectively, and the tensor field  $\sigma_A(\vec{x})$  corresponds to the active stress profile, as specified above (Figure S7B). To define these fields mathematically, it is necessary to find the minimal distance of any point in the tissue to the tissue surface. In order to determine the minimal distance of any given point  $\vec{x}$  in the tissue to the surface, we use the general extrusion operator in COMSOL Multiphysics, which calculates the minimal distance  $x_m$  of the point  $\vec{x}$  to the surface. Therefore, to generate the profiles in Figure S7B (or in Figure 5), it is necessary to define a function with two regions: one for distances from the tissue surface smaller than  $\lambda$  ( $x_m < \lambda$ ; the progenitor region) and one for distances larger than  $\lambda$  ( $x_m > \lambda$ ; the region of committed chondrocytes). Since the transition from one region to the other is not infinitely sharp, but it rather occurs over a finite size, we introduced the length scale  $a$ , which is the transition length scale characterizing the distance over which the different input fields transit from one behavior to the other (Figure S7B). Knowing the minimal distance of any point in the tissue to the tissue surface, we define the input functions as follows (all only dependent on the distance to the tissue surface,  $x_m$ . The cell proliferation profile,  $Q(\vec{x})$ , is given by

10

15

20

$$Q(x_m) = Q_0 \frac{1}{1 + \exp\left(\frac{x_m - \lambda}{a}\right)} \quad (S5)$$

where  $Q_0$  is the maximal cell proliferation rate as seen in Figure S7B. The active stress tensor,  $\sigma_A(\vec{x})$ , is given by

25

$$\sigma_A(x_m) = \begin{pmatrix} A(x_m) & 0 \\ 0 & 0 \end{pmatrix} \quad (S6)$$

where the axial active stress in the direction perpendicular to the PD axis,  $A(x_m)$ , reads

$$A(x_m) = \frac{\alpha \sigma_A^0}{1 + \exp\left(\frac{x_m - \lambda}{a}\right)} + \frac{\sigma_A^0}{1 + \exp\left(\frac{\lambda - x_m}{a}\right)} \quad (S7)$$

with  $\sigma_A^0$  being the maximal active stress and  $\alpha$  being the fraction of active stress that acts in the progenitor region ( $\alpha = 0.1$  in all simulations; a different value of  $\alpha$  does not change the qualitative results of the simulations, as long as it is smaller than 1) as seen in Figure S7B. Finally, the spatial distribution of the tissue viscosity (Figure S7B) reads

30

35

$$\mu(x_m) = \frac{\mu_F}{1 + \exp\left(\frac{x_m - \lambda}{a}\right)} + \frac{\mu_S}{1 + \exp\left(\frac{\lambda - x_m}{a}\right)} \quad (S8)$$

where  $\mu_F$  and  $\mu_S$  are the viscosities in fluid-like region and the solid-like region, respectively as seen in Figure S7B.

Once all the input fields were specified, we used COMSOL Multiphysics 5.3 to perform a Finite Element simulations of the system described above. We initialized the simulation with a tissue shaped as a semi-circle (initial condition for the tissue shape; Figure S7C) in a

40

box of fluid with negligible viscosity compared to the tissue (such as tissue culture media) with  $x$  and  $y$  defining the anteroposterior (AP) and proximal distal (PD) axes, respectively (Figure S7C). The simulation box was made much larger than the tissue size (by at least a factor of 10) to avoid any undesired boundary effects. We mechanically support the tissue at its most proximal end with a large region of viscosity  $\mu_P$ , which was assumed to be constant in the simulations,  $\mu_P = 2\mu_F$ . The two ends of the semi-circle are in contact with this proximal fluid region of intermediate viscosity (Figure S7C'). Flow is allowed through the boundaries of the simulating box, except at the bottom end, where no flow is allowed to go through to reflect the presence of the body at this end. For any given simulation, the spatial profiles of cell proliferation, active stress tensor, and viscosity were provided as inputs to the simulation. In COMSOL, the input functions are written as piecewise functions with a user-defined transition region (of size  $a$ , as described above). Once the initial system was set, we defined an adaptive finite element mesh in COMSOL that was thereafter dynamically refined as the digit shape evolved in order to properly resolve fine features in the tissue shape, morphogenetic flows and stress fields (Figure S7C''). The simulations predict the shape of the extending tissue, the morphogenetic flows (velocity field) and the (passive) stress fields that result from the given inputs according to fundamental physical laws (force and mass balance).

After normalizing all variables, the system is characterized by four dimensionless parameters that control the different possible behaviors. First, the ratio of surface stresses  $\sigma_C \equiv \gamma/\lambda$  associated with tissue surface tension and shear stresses associated with tissue flows in the fluid-like region  $\sigma_{SF} \equiv \mu_f/(\rho/Q_0)$ , namely  $\sigma_C/\sigma_{SF}$ . A value of  $\sigma_C/\sigma_{SF} = 4.8$  provided good agreement between simulations and experimental data for all conditions. Second, the ratio of the viscosities in the tissue region of committed chondrocytes and the progenitor region, namely  $\mu_S/\mu_F$ . We found that the ratio  $\mu_S/\mu_F = 10$  reproduces well the wild type and Wnt5a mutant data. Third, the ratio of the maximal active stress,  $\sigma_A^0$ , to the ratio of the shear stresses associated with tissue flows, namely  $\sigma_A^0/\sigma_{SF}$ . We found that a ratio  $\sigma_A^0/\sigma_{SF} = 8$  reproduces well the tissue flows observed in wild type digits. For Wnt5a mutant embryos, we set the active stress to zero everywhere in the tissue ( $\sigma_A^0/\sigma_{SF} = 0$ ) following our experimental observations.

To theoretically account for the experimental observation suggesting that the stress localization could define the PFR/DC and drive Sox9 expression, leading to mesenchymal condensation and the rigidification of the tissue, we implemented a mechanical feedback in the simulations. This was done by coupling the maximal AP stress,  $\sigma_{AP}^{\max}$ , to the length scale of the transition region of the input functions,  $a$ , as the smoothness of the transition depends on the degree to which progenitor cells commit to a chondrogenic fate. A high maximal AP stress leads to smaller transition region (smaller  $a$ ) because progenitor cells commit at a higher rate, whereas low maximal AP stress leads to a larger transition region (larger  $a$ ) because progenitor cells commit at a smaller percentage or take longer to commit. To implement this mechanical feedback, the simulations were run for a short time interval ( $\Delta t = 0.1 \tau$ , with  $\tau$  being the characteristic time scale of the tissue growth, namely  $\tau \equiv \rho/Q_0$ ) with an initial value of  $a$  ( $a = a_0$ ). The value of  $a$  after the first iteration was subsequently updated as

$$a(t) = a_0 \left( \frac{\sigma_{AP|t=0.1}^{\max, WT}}{\sigma_{AP|t}^{\max}} \right)^\beta \quad (S9)$$

where  $\beta$  is an adjustable parameter (which we fixed to  $\beta = 0.5$  in all simulations),  $\sigma_{AP|t=0.1}^{\max,WT}$  is the maximal AP stress after the first iteration in the WT case, and  $\sigma_{AP|t}^{\max}$  is the maximal AP stress at time  $t$ . Simulating the system (both for WT or Wnt5a mutants) with this mechanical feedback led to solutions with nearly constant values of the transition lengthscale  $a$  after an initial transient regime, reaching a near steady-state growth of the digit for the simulated timeframe.

## QUANTIFICATION AND STATISTICAL ANALYSIS

10

For quantification of individual cell tracking, cell division, and PIV analysis, see subheading *Live imaging and image analysis* in the section METHOD DETAILS of this STAR METHODS. Statistical details of experiments can be found in the legends of the figures in which the relevant results are presented.

15

## Supplemental Information legends

### Legends for supplementary videos

5 **Video S1. Morphogenetic flows in an E11.5 (+ 20h) WT developing digit.** Related to Figure 1. Left panel: time-lapse movie of an E11.5+20h *Rosa<sup>mTmG/mTmG</sup>* digit, reporting cell membranes, acquired every 12 min for 16h. Manually tracked cells are displayed using colored dots. Right panel: corresponding velocity fields, obtained by PIV (n=3 limbs). Scale bar is 50  $\mu\text{m}$ .

10 **Video S2. SOX9 expression and PIV in a WT developing digit.** Related to Figure 1. Left panel: time-lapse movie of an E11.5+20h *Sox9<sup>IRES-GFP/IRES-GFP</sup>* digit, reporting *Sox9* expression, acquired every 30 min for 12h. Right panel: corresponding velocity fields, obtained by PIV (n=2 limbs). Scale bar is 50  $\mu\text{m}$ .

15 **Video S3. Cell division in a WT developing digit.** Related to Figure 1. **A**, Time series projection of an E11.5+20h *Rosa<sup>mTmG/mTmG</sup>* digit, reporting cell membranes, acquired every 12 min for 16h. Cell division events are mapped using red lines to highlight the orientation of cell separation. **B**, Cell division orientation plotted by region: SOX9<sup>-</sup> progenitors (distal) and SOX9<sup>+</sup> differentiating and differentiated cells (proximal). SOX9<sup>+</sup> cells show an AP bias. **C**. Examples of cell divisions in distal progenitors (top) and proximal SOX9<sup>+</sup> cells (bottom). In the proximal region, cell division  
20 occurs along the AP axis and is followed by re-intercalation of daughter cells (n=4 limbs).

**Video S4. Differential cell behavior along the PD axis.** Related to Figure 1. Higher magnification of different regions along the PD axis, from supplementary video 1 and as shown in Figure 1D-H. **A**, Distal region: SOX9<sup>-</sup> progenitors showing rapid disorganized motion. Most cells cannot be tracked during the entire duration (4h) of the movie as they  
25 move out of the focal plane (i.e. DV axis). **B**, Intermediate region: As cells initiate SOX9 expression, they intercalate along the mediolateral (AP) axis. **C**, Proximal region: SOX9<sup>+</sup> committed chondrocytes do not exchange neighbors and display coherent movement proximally. Scale bars on the top panels are 50  $\mu\text{m}$  and in the middle panels are 10  $\mu\text{m}$ .

30 **Video S5. Morphogenetic flows in an E12.5 (+ 20h) WT developing digit.** Related to Figure 1. Left panel: time-lapse movie of an E12.5 + 20h *Rosa<sup>mTmG/mTmG</sup>* digit, reporting cell membranes, acquired every 12 min for 18h. Manually tracked cells are displayed using colored dots. Right panel: corresponding velocity fields, obtained by PIV (n=2 limbs). Scale bar is 50  $\mu\text{m}$ .

35 **Video S6. Disrupted morphogenetic flows in a *Wnt5a*<sup>-/-</sup> developing limb.** Related to Figure 2. Left panel: time-lapse imaging of an E12.5 + 20h *Wnt5a*<sup>-/-</sup>; *Rosa<sup>mTmG/mTmG</sup>* digit, reporting cell membranes in absence of *Wnt5a* expression, acquired every 12 min for 3.2h. Individual cell tracking overlaid as colored dots. Note the poor signal-to-noise ratio of the memtdTomato in the proximal-most region (lower part), corresponding to the metacarpal primordium. Right panel: corresponding velocity fields,  
40 obtained by PIV (n=3 mutant limbs). Scale bar 50  $\mu\text{m}$ .

**Video S7. Disrupted morphogenetic flows in a H1152-treated digit.** Related to Figure 6. Left panel: time-lapse movie of an E12 + 20h *Rosa<sup>mTmG/mTmG</sup>* digit, reporting cell membranes and treated with the Rock inhibitor H1152, acquired every 12 min for 5h. Right panel:

corresponding velocity fields, obtained by PIV (n=3 H1152-treated limbs). Scale bar is 100  $\mu\text{m}$ .

5

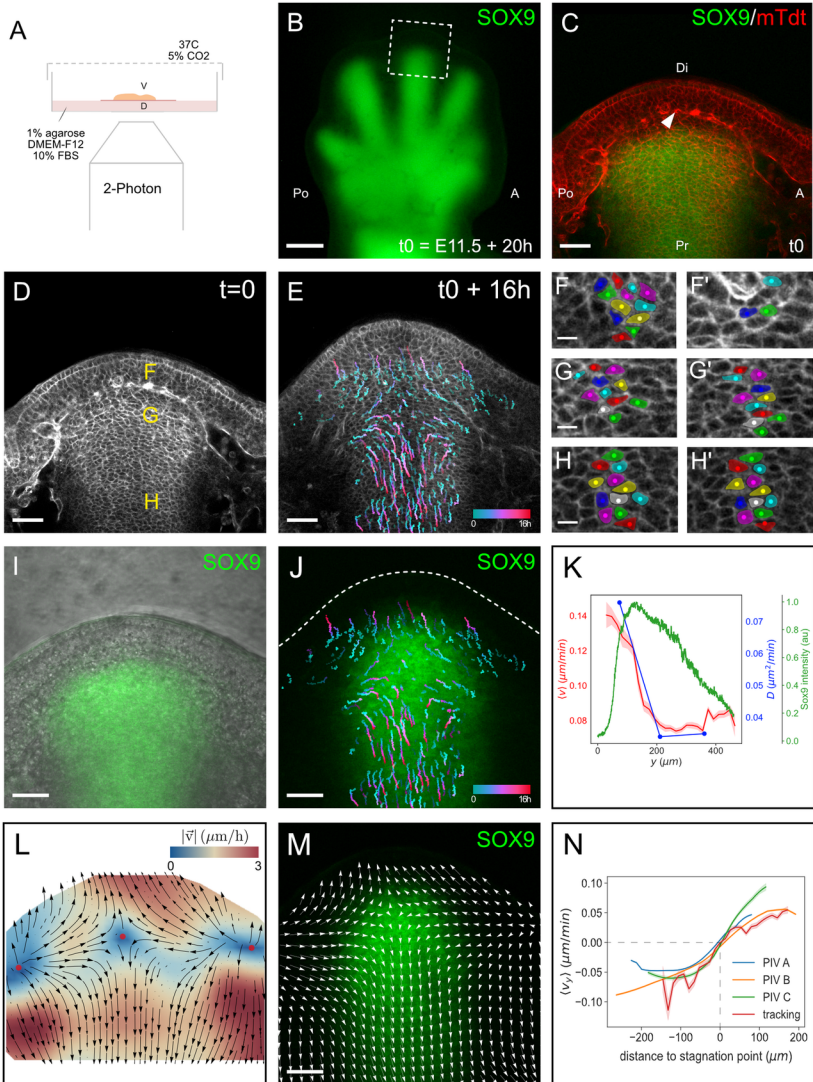
## References

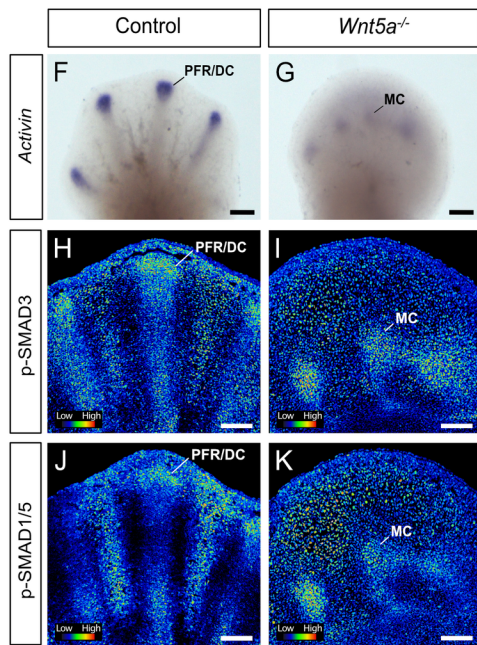
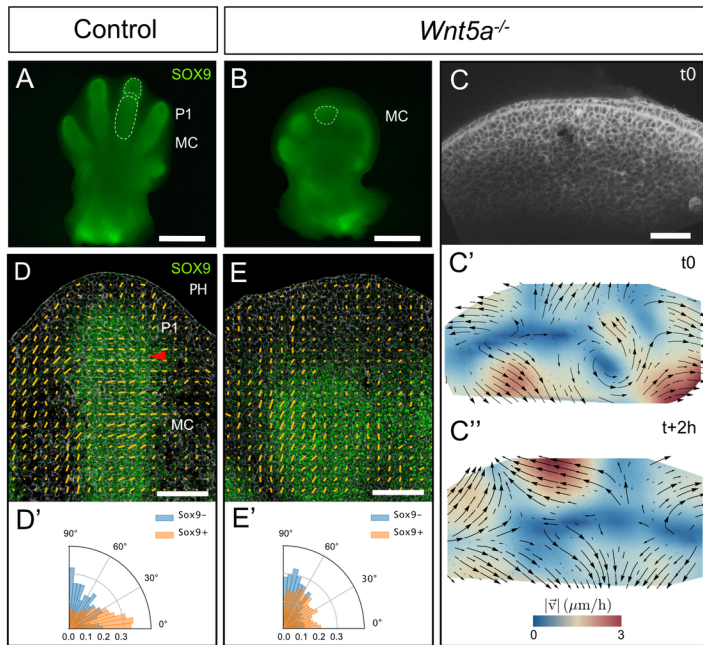
- 5 Akiyama, H., Chaboissier, M.-C., Martin, J.F., Schedl, A., de Crombrughe, B., 2002. The transcription factor Sox9 has essential roles in successive steps of the chondrocyte differentiation pathway and is required for expression of Sox5 and Sox6. *Genes Dev* 16, 2813–2828. <https://doi.org/10.1101/gad.1017802>
- Banavar, S.P., Carn, E.K., Rowghanian, P., Stooke-Vaughan, G., Kim, S., Campàs, O., 2021. Mechanical control of tissue shape and morphogenetic flows during vertebrate body axis elongation. *Sci Rep* 11, 8591. <https://doi.org/10.1038/s41598-021-87672-3>
- 10 Barriga, E.H., Franze, K., Charras, G., Mayor, R., 2018. Tissue stiffening coordinates morphogenesis by triggering collective cell migration in vivo. *Nature* 554, 523–527. <https://doi.org/10.1038/nature25742>
- Baur, S.T., Mai, J.J., Dymecki, S.M., 2000. Combinatorial signaling through BMP receptor IB and GDF5: shaping of the distal mouse limb and the genetics of distal limb diversity. *Development* 127, 605–619.
- Boehm, B., Rautschka, M., Quintana, L., Raspopovic, J., Jan, Ž., Sharpe, J., 2011. A landmark-free morphometric staging system for the mouse limb bud. *Development* 138, 1227. <https://doi.org/10.1242/dev.057547>
- 20 Campàs, O., Mammoto, T., Hasso, S., Sperling, R.A., O’Connell, D., Bischof, A.G., Maas, R., Weitz, D.A., Mahadevan, L., Ingber, D.E., 2014. Quantifying cell-generated mechanical forces within living embryonic tissues. *Nat Methods* 11, 183–189. <https://doi.org/10.1038/nmeth.2761>
- Chan, H.Y., Sivakamasundari, V., Xing, X., Kraus, P., Yap, S.P., Ng, P., Lim, S.L., Lufkin, T., 2011. Comparison of IRES and F2A-Based Locus-Specific Multicistronic Expression in Stable Mouse Lines. *PLOS ONE* 6, e28885. <https://doi.org/10.1371/journal.pone.0028885>
- 25 Chaudhuri, O., Cooper-White, J., Janmey, P.A., Mooney, D.J., Shenoy, V.B., 2020. Effects of extracellular matrix viscoelasticity on cellular behaviour. *Nature* 584, 535–546. <https://doi.org/10.1038/s41586-020-2612-2>
- 30 Dickinson, R., Tranquillo, R., 1993. Optimal estimation of cell movement indices from the statistical analysis of cell tracking data. *Aiche Journal* 39, 1995–2010.
- Durande, M., Tlili, S., Homan, T., Guirao, B., Graner, F., Delanoë-Ayari, H., 2019. Fast determination of coarse-grained cell anisotropy and size in epithelial tissue images using Fourier transform. *Phys. Rev. E* 99, 062401. <https://doi.org/10.1103/PhysRevE.99.062401>
- 35 Engler, A.J., Sen, S., Sweeney, H.L., Discher, D.E., 2006. Matrix Elasticity Directs Stem Cell Lineage Specification. *Cell* 126, 677–689. <https://doi.org/10.1016/j.cell.2006.06.044>
- Gao, B., Ajima, R., Yang, W., Li, C., Song, H., Anderson, M.J., Liu, R.R., Lewandoski, M.B., Yamaguchi, T.P., Yang, Y., 2018. Coordinated directional outgrowth and pattern formation by integration of Wnt5a and Fgf signaling in planar cell polarity. *Development* 145. <https://doi.org/10.1242/dev.163824>
- 40 Gao, B., Song, H., Bishop, K., Elliot, G., Garrett, L., English, M.A., Andre, P., Robinson, J., Sood, R., Minami, Y., Economides, A.N., Yang, Y., 2011. Wnt signaling gradients establish planar cell polarity by inducing Vangl2 phosphorylation through Ror2. *Dev Cell* 20, 163–176. <https://doi.org/10.1016/j.devcel.2011.01.001>
- 45 Gros, J., Hu, J.K.-H., Vinegoni, C., Feruglio, P.F., Weissleder, R., Tabin, C.J., 2010. WNT5A/JNK and FGF/MAPK pathways regulate the cellular events shaping the

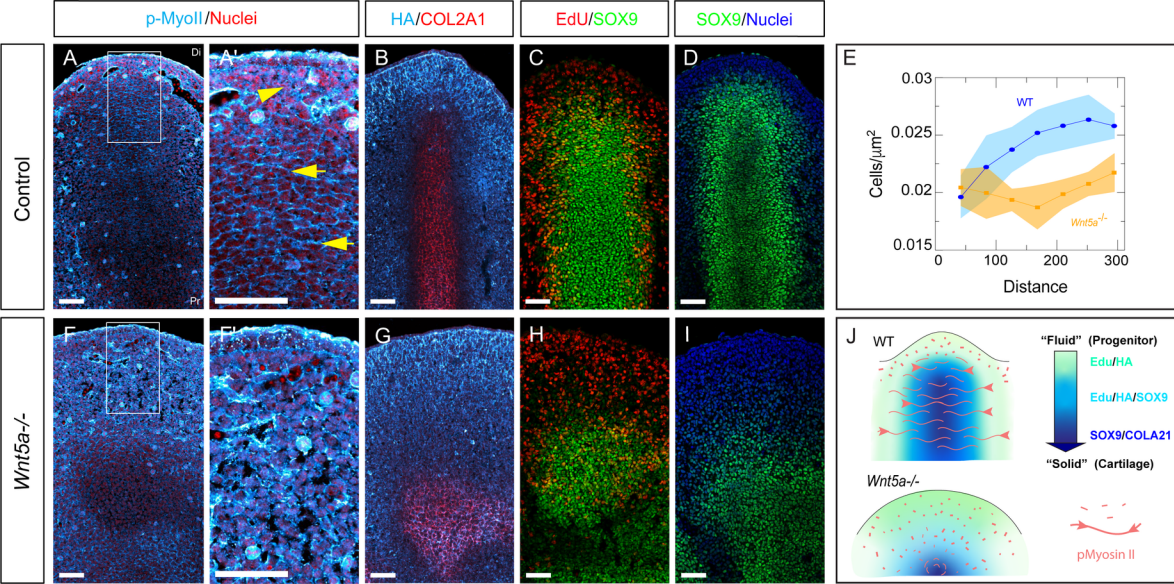
- vertebrate limb bud. *Curr Biol* 20, 1993–2002.  
<https://doi.org/10.1016/j.cub.2010.09.063>
- Hannezo, E., Heisenberg, C.-P., 2019. Mechanochemical Feedback Loops in Development and Disease. *Cell* 178, 12–25. <https://doi.org/10.1016/j.cell.2019.05.052>
- 5 Harris, C.R., Millman, K.J., van der Walt, S.J., Gommers, R., Virtanen, P., Cournapeau, D., Wieser, E., Taylor, J., Berg, S., Smith, N.J., Kern, R., Picus, M., Hoyer, S., van Kerkwijk, M.H., Brett, M., Haldane, A., del Río, J.F., Wiebe, M., Peterson, P., Gérard-Marchant, P., Sheppard, K., Reddy, T., Weckesser, W., Abbasi, H., Gohlke, C., Oliphant, T.E., 2020. Array programming with NumPy. *Nature* 585, 357–362.  
 10 <https://doi.org/10.1038/s41586-020-2649-2>
- Hiscock, T.W., Tschopp, P., Tabin, C.J., 2017. On the Formation of Digits and Joints during Limb Development. *Dev Cell* 41, 459–465.  
<https://doi.org/10.1016/j.devcel.2017.04.021>
- 15 Huang, B.-L., Trofka, A., Furusawa, A., Norrie, J.L., Rabinowitz, A.H., Vokes, S.A., Mark Taketo, M., Zakany, J., Mackem, S., 2016. An interdigit signalling centre instructs coordinate phalanx-joint formation governed by 5'Hoxd–Gli3 antagonism. *Nature Communications* 7, 12903. <https://doi.org/10.1038/ncomms12903>
- Juhász, T., Matta, C., Somogyi, C., Katona, É., Takács, R., Soha, R.F., Szabó, I.A., Cserháti, C., Szödy, R., Karácsonyi, Z., Bakó, É., Gergely, P., Zákány, R., 2014. Mechanical loading stimulates chondrogenesis via the PKA/CREB-Sox9 and PP2A pathways in chicken micromass cultures. *Cellular Signalling* 26, 468–482.  
 20 <https://doi.org/10.1016/j.cellsig.2013.12.001>
- Kavanagh, K.D., Shoval, O., Winslow, B.B., Alon, U., Leary, B.P., Kan, A., Tabin, C.J., 2013. Developmental bias in the evolution of phalanges. *Proc Natl Acad Sci USA* 201315213. <https://doi.org/10.1073/pnas.1315213110>
- 25 Li, Y., Dudley, A.T., 2009. Noncanonical frizzled signaling regulates cell polarity of growth plate chondrocytes. *Development* 136, 1083. <https://doi.org/10.1242/dev.023820>
- Lucio, A.A., Mongera, A., Shelton, E., Chen, R., Doyle, A.M., Campàs, O., 2017. Spatiotemporal variation of endogenous cell-generated stresses within 3D multicellular spheroids. *Sci Rep* 7, 12022. <https://doi.org/10.1038/s41598-017-12363-x>
- 30 Merino, R., Macias, D., Ganan, Y., Rodriguez-Leon, J., Economides, A.N., Rodriguez-Esteban, C., Izpisua-Belmonte, J.C., Hurlé, J.M., 1999. Control of digit formation by activin signalling. *Development* 126, 2161–2170.  
 35 <https://doi.org/10.1242/dev.126.10.2161>
- Mongera, A., Rowghanian, P., Gustafson, H.J., Shelton, E., Kealhofer, D.A., Carn, E.K., Serwane, F., Lucio, A.A., Giammona, J., Campàs, O., 2018. A fluid-to-solid jamming transition underlies vertebrate body axis elongation. *Nature* 561, 401–405.  
<https://doi.org/10.1038/s41586-018-0479-2>
- 40 Montero, J.A., Hurlé, J.M., 2007. Deconstructing digit chondrogenesis. *Bioessays* 29, 725–737. <https://doi.org/10.1002/bies.20607>
- Montero, J.A., Lorda-Diez, C.I., Francisco-Morcillo, J., Chimal-Monroy, J., Garcia-Porrero, J.A., Hurlé, J.M., 2017. Sox9 Expression in Amniotes: Species-Specific Differences in the Formation of Digits. *Front Cell Dev Biol* 5, 23–23.  
 45 <https://doi.org/10.3389/fcell.2017.00023>
- Montero, J.A., Lorda-Diez, C.I., Gañan, Y., Macias, D., Hurlé, J.M., 2008. Activin/TGFβ and BMP crosstalk determines digit chondrogenesis. *Developmental Biology* 321, 343–356. <https://doi.org/10.1016/j.ydbio.2008.06.022>

- Muzumdar, M.D., Tasic, B., Miyamichi, K., Li, L., Luo, L., 2007. A global double-fluorescent Cre reporter mouse. *genesis* 45, 593–605. <https://doi.org/10.1002/dvg.20335>
- 5 Newman, S., Frisch, H., 1979. Dynamics of skeletal pattern formation in developing chick limb. *Science* 205, 662–668. <https://doi.org/10.1126/science.462174>
- Newville, M., Stensitzki, T., Allen, D.B., Rawlik, M., Ingargiola, A., Nelson, A., 2016. Lmfit: Non-Linear Least-Square Minimization and Curve-Fitting for Python.
- Pryce, B.A., Watson, S.S., Murchison, N.D., Staverosky, J.A., Dünker, N., Schweitzer, R., 10 2009. Recruitment and maintenance of tendon progenitors by TGFbeta signaling are essential for tendon formation. *Development* 136, 1351–1361. <https://doi.org/10.1242/dev.027342>
- Raspopovic, J., Marcon, L., Russo, L., Sharpe, J., 2014. Digit patterning is controlled by a Bmp-Sox9-Wnt Turing network modulated by morphogen gradients. *Science* 345, 566. <https://doi.org/10.1126/science.1252960>
- 15 Romereim, S.M., Conoan, N.H., Chen, B., Dudley, A.T., 2014. A dynamic cell adhesion surface regulates tissue architecture in growth plate cartilage. *Development* 141, 2085. <https://doi.org/10.1242/dev.105452>
- Saadaoui, M., Rocancourt, D., Roussel, J., Corson, F., Gros, J., 2020. A tensile ring drives tissue flows to shape the gastrulating amniote embryo. *Science* 367, 453. <https://doi.org/10.1126/science.aaw1965>
- 20 Schneider, C.A., Rasband, W.S., Eliceiri, K.W., 2012. NIH Image to ImageJ: 25 years of image analysis. *Nat Methods* 9, 671–675. <https://doi.org/10.1038/nmeth.2089>
- Sheth, R., Marcon, L., Bastida, M.F., Junco, M., Quintana, L., Dahn, R., Kmita, M., Sharpe, J., Ros, M.A., 2012. Hox genes regulate digit patterning by controlling the wavelength of a Turing-type mechanism. *Science* 338, 1476–1480. <https://doi.org/10.1126/science.1226804>
- 25 Sletten, E.M., Swager, T.M., 2014. Fluorofluorophores: Fluorescent Fluorous Chemical Tools Spanning the Visible Spectrum. *J. Am. Chem. Soc.* 136, 13574–13577. <https://doi.org/10.1021/ja507848f>
- 30 Solis, M.A., Chen, Y.-H., Wong, T.Y., Bittencourt, V.Z., Lin, Y.-C., Huang, L.L.H., 2012. Hyaluronan Regulates Cell Behavior: A Potential Niche Matrix for Stem Cells. *Biochem Res Int* 2012. <https://doi.org/10.1155/2012/346972>
- Stooke-Vaughan, G.A., Campàs, O., 2018. Physical control of tissue morphogenesis across scales. *Current Opinion in Genetics & Development* 51, 111–119. <https://doi.org/10.1016/j.gde.2018.09.002>
- 35 Suzuki, T., Hasso, S.M., Fallon, J.F., 2008. Unique SMAD1/5/8 activity at the phalanx-forming region determines digit identity. *Proc Natl Acad Sci USA* 105, 4185. <https://doi.org/10.1073/pnas.0707899105>
- Takahashi, I., Nuckolls, G.H., Takahashi, K., Tanaka, O., Semba, I., Dashner, R., Shum, L., Slavkin, H.C., 1998. Compressive force promotes sox9, type II collagen and aggrecan and inhibits IL-1beta expression resulting in chondrogenesis in mouse embryonic limb bud mesenchymal cells. *J. Cell Sci.* 111, 2067.
- 40 Tanaka, S., 2015. Simulation Frameworks for Morphogenetic Problems. *Computation* 3, 197–221. <https://doi.org/10.3390/computation3020197>
- 45 Tanck, E., Van Donkelaar, C.C., Jepsen, K.J., Goldstein, S.A., Weinans, H., Burger, E.H., Huiskes, R., 2004. The mechanical consequences of mineralization in embryonic bone. *Bone* 35, 186–190. <https://doi.org/10.1016/j.bone.2004.02.015>
- Topol, L., Jiang, X., Choi, H., Garrett-Beal, L., Carolan, P.J., Yang, Y., 2003. Wnt-5a inhibits the canonical Wnt pathway by promoting GSK-3-independent  $\beta$ -catenin degradation. *Journal of Cell Biology* 162, 899–908. <https://doi.org/10.1083/jcb.200303158>
- 50

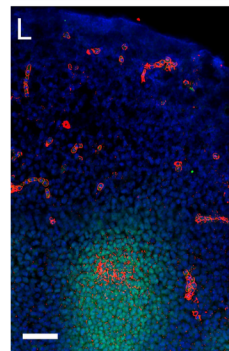
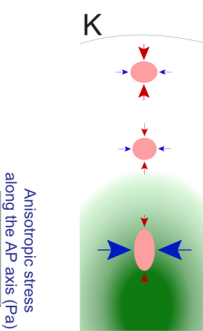
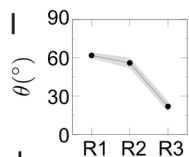
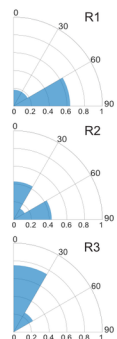
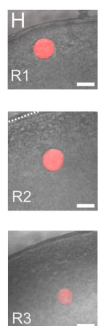
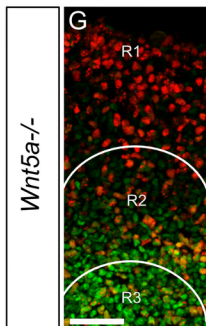
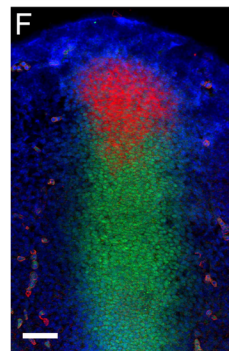
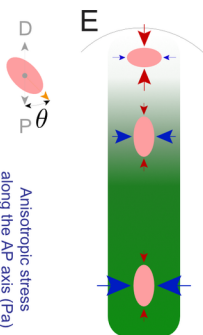
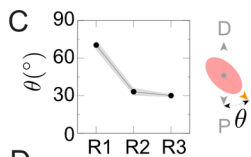
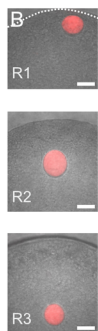
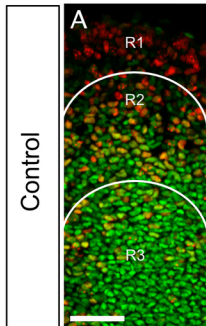
- Turing Alan Mathison, 1952. The chemical basis of morphogenesis. *Philosophical Transactions of the Royal Society of London. Series B, Biological Sciences* 237, 37–72. <https://doi.org/10.1098/rstb.1952.0012>
- 5 Wang, B., Sinha, T., Jiao, K., Serra, R., Wang, J., 2011. Disruption of PCP signaling causes limb morphogenesis and skeletal defects and may underlie Robinow syndrome and brachydactyly type B. *Hum Mol Genet* 20, 271–285. <https://doi.org/10.1093/hmg/ddq462>
- 10 Witte, F., Chan, D., Economides, A.N., Mundlos, S., Stricker, S., 2010. Receptor tyrosine kinase-like orphan receptor 2 (ROR2) and Indian hedgehog regulate digit outgrowth mediated by the phalanx-forming region. *Proc Natl Acad Sci USA* 107, 14211. <https://doi.org/10.1073/pnas.1009314107>
- 15 Wyczalkowski, M.A., Chen, Z., Filas, B.A., Varner, V.D., Taber, L.A., 2012. Computational models for mechanics of morphogenesis. *Birth Defects Res C Embryo Today* 96, 132–152. <https://doi.org/10.1002/bdrc.21013>
- 20 Wyngaarden, L.A., Vogeli, K.M., Ciruna, B.G., Wells, M., Hadjantonakis, A.-K., Hopyan, S., 2010. Oriented cell motility and division underlie early limb bud morphogenesis. *Development* 137, 2551. <https://doi.org/10.1242/dev.046987>
- 25 Yamaguchi, T.P., Bradley, A., McMahon, A.P., Jones, S., 1999. A Wnt5a pathway underlies outgrowth of multiple structures in the vertebrate embryo. *Development* 126, 1211.
- 30 Yi, S.E., Daluiski, A., Pederson, R., Rosen, V., Lyons, K.M., 2000. The type I BMP receptor BMPRII is required for chondrogenesis in the mouse limb. *Development* 127, 621–630. <https://doi.org/10.1242/dev.127.3.621>
- 35 Zhu, X., Zhu, H., Zhang, L., Huang, S., Cao, J., Ma, G., Feng, G., He, L., Yang, Y., Guo, X., 2012. Wls-mediated Wnts differentially regulate distal limb patterning and tissue morphogenesis. *Developmental Biology* 365, 328–338. <https://doi.org/10.1016/j.ydbio.2012.02.019>



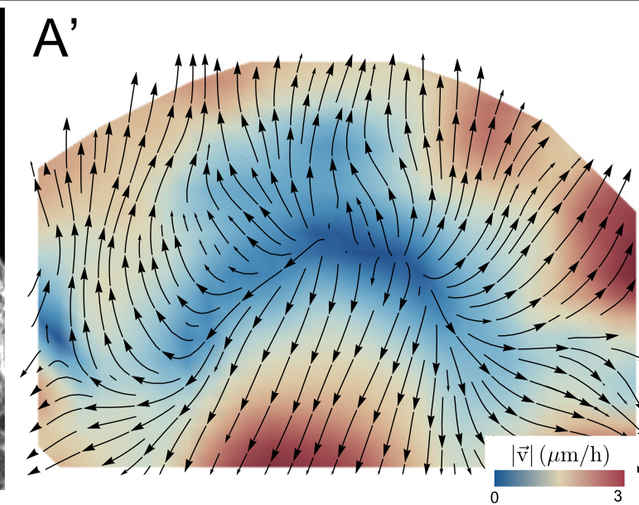
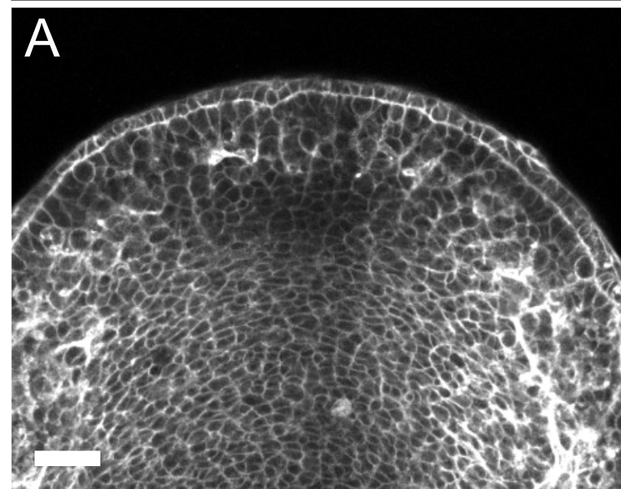




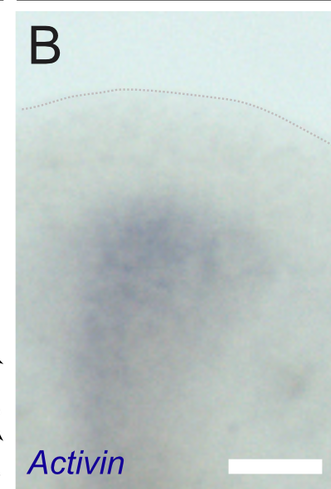


**EdU/SOX9****Endogenous Stress Measurements****Activin/SOX9**

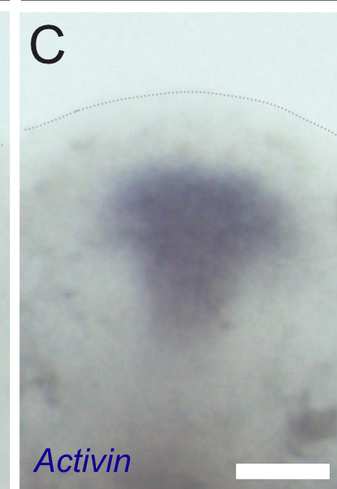
H1152



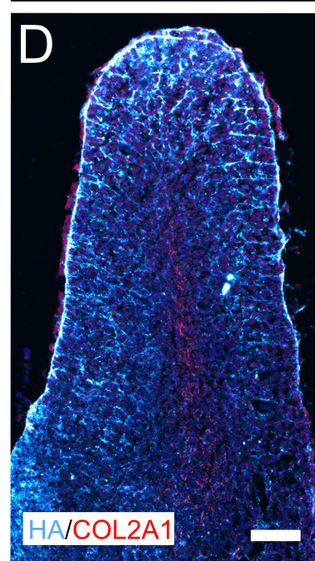
H1152



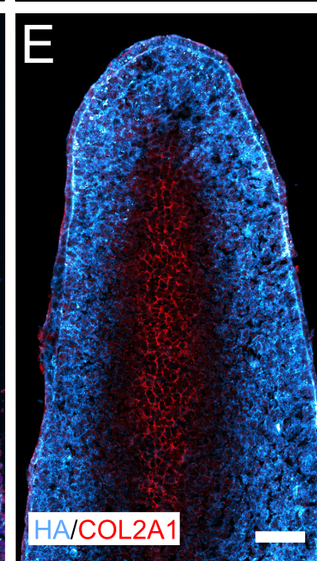
Control



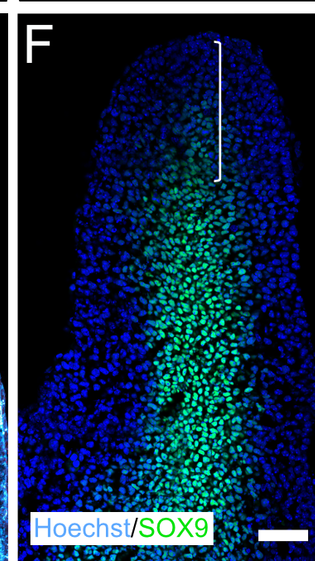
H1152



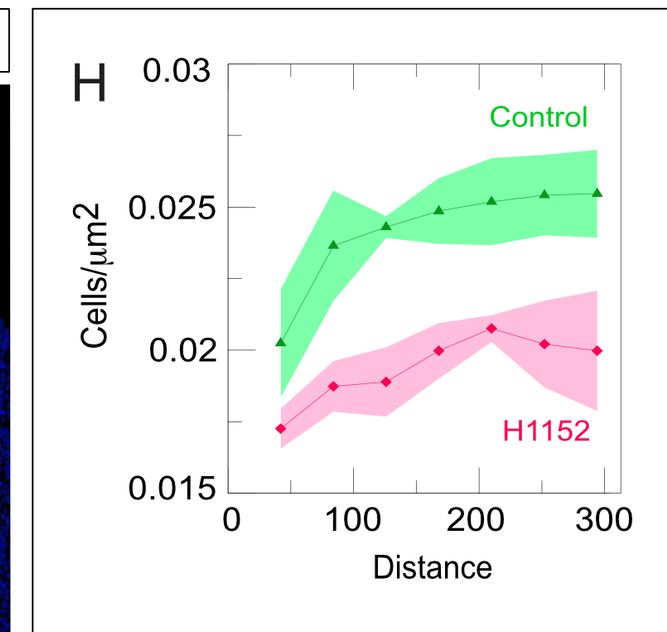
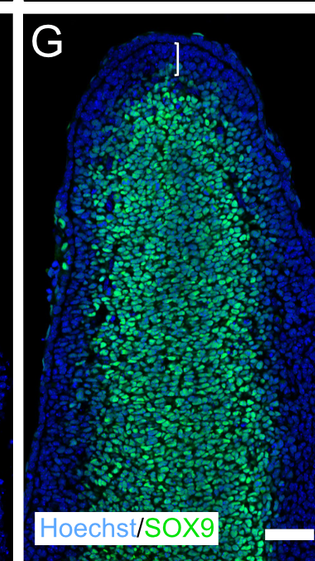
Control



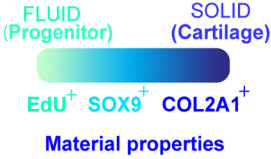
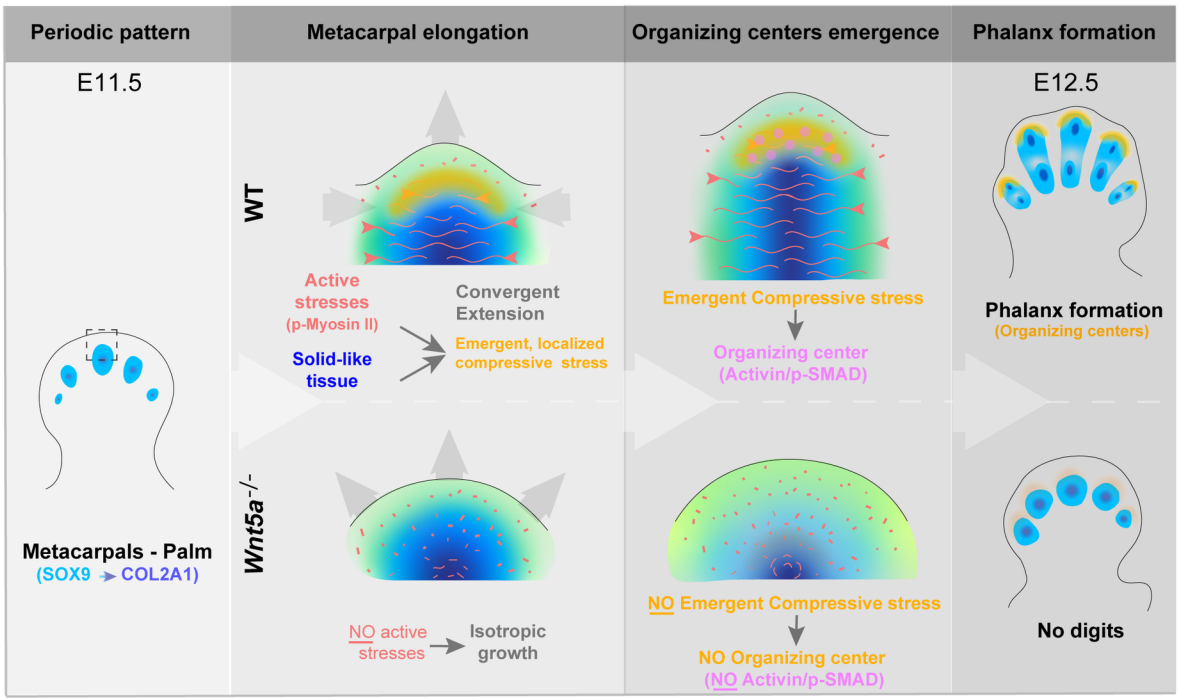
H1152



Control



A



B

